The role of electrode wettability in electrochemical reduction of carbon dioxide

Li, Mengran; Idros, Mohamed Nazmi; Wu, Yuming; Burdyny, Thomas; Garg, Sahil; Zhao, Xiu Song; Wang, Geoff; Rufford, Thomas E.

DOI
10.1039/d1ta03636j

Publication date
2021

Document Version
Accepted author manuscript

Published in
Journal of Materials Chemistry A

The role of electrode wettability in electrochemical reduction of carbon dioxide

Mengran Li*[a,b†], Mohamed Nazmi Idros[a,†], Yuming Wu[a], Thomas Burdyny[b], Sahil Garg[c], Xiu Song Zhao[a], Geoff Wang[a], Thomas E. Rufford[a,*]

a. School of Chemical Engineering, the University of Queensland, St Lucia, 4072, Brisbane, Queensland, Australia

b. Materials for Energy Conversion and Storage (MECS), Department of Chemical Engineering, Faculty of Applied Sciences, Delft University of Technology, van der Maasweg 9, 2629 HZ Delft, The Netherlands

c. Surface Physics and Catalysis (SurfCat) Section, Department of Physics, Technical University of Denmark, 2800 Kgs. Lyngby, Denmark

† M.Li. and M.N. Idros contributed equally to this work.

Corresponding authors: M. Li: m.li6@uq.edu.au; T.E. Rufford: t.rufford@uq.edu.au

Abstract

The electrochemical reduction of carbon dioxide (CO_2RR) requires access to ample gaseous CO_2 and liquid water to fuel reactions at high current densities for industrial-scale applications. Substantial improvement of the CO_2RR rate has largely arisen from positioning the catalyst close to gas-liquid interfaces, such as in gas-diffusion electrodes. These requirements add complexity to an electrode design that no longer consists of only a catalyst but also a microporous and nanoporous network of gas-liquid-solid interfaces of the electrode. In this three-dimensionl structure, electrode wettability plays a pivotal role in the CO_2RR because the affinity of the electrode surface by water impacts the observed electrode reactivity, product selectivity, and long-term stability. All these performance metrics are critical in an industrial electrochemical process. This review provides an in-depth analysis of electrode wettability's role in achieving an efficient, selective, and stable CO_2RR performance. We first discuss the underlying mechanisms of electrode wetting phenomena and the foreseen ideal wetting conditions for the CO_2RR. Then we summarize recent advances in improving cathode performance by altering the wettability of the catalyst layer of gas-diffusion electrodes. We conclude the review by discussing the current challenges and opportunities to develop efficient and selective cathode for CO_2RR at industrially relevant rates. The insights generated from this review could also benefit the advancement of other critical electrochemical processes that involve multiple complex flows in porous electrodes, such as electrochemical reduction of carbon monoxide, oxygen, and nitrogen.

Keywords: CO_2 electrochemical reduction; wettability; catalyst; electrolyte; gas-diffusion electrode

Table of Content

ABSTRACT **1**

TABLE OF CONTENT **2**

1. INTRODUCTION **3**

2. FUNDAMENTALS OF WETTING **7**

2.1 STATIC WETTING AND CAPILLARY PRESSURE 7

2.2 WETTING UNDER ELECTRIC FIELD 9

2.3 EFFLORESCENCE AT CO_2RR GAS-DIFFUSION CATHODE 13

2.4 DESIRED WETTING CONDITIONS FOR CO_2RR GAS-DIFFUSION CATHODES 14

3. IMPROVING CO_2RR PERFORMANCE BY MANIPULATING WETTABILITY **18**

3.1 THE ROLE OF LIQUID IN ELECTRODE WETTABILITY 18

3.2 THE ROLE OF SOLID PHASE IN ELECTRODE WETTABILITY 21

Metal-based materials *21*

Carbon-based materials *23*

Organic additives – binders and ionomers *23*

3.3 MODIFY THE GAS-DIFFUSION LAYERS 24

Carbon-based GDLs *24*

Non-carbon based GDLs *36*

3.4 TUNE THE CATALYST LAYER WETTABILITY 42

Reduce catalyst overpotential *42*

Addition of hydrophobic materials in the CLs *45*

Addition of ionomers in the CLs *47*

Addition of organic modifiers *50*

4. CONCLUSIONS AND OUTLOOK **54**

OUTLOOK 55

ACKNOWLEDGMENT 58

DECLARATION OF INTEREST 58

LIST OF ACRONYMS 58

5. REFERENCES **58**

1. Introduction

A low-temperature carbon dioxide (CO_2) electrolyzer is a technology that uses electricity to convert CO_2 into chemicals and fuels, such as formic acid (HCOOH), carbon monoxide (CO), methane (CH_4), and multicarbon products (e.g., ethylene (C_2H_4), ethanol (C_2H_5OH), and propanol (C_3H_8O)). As the cost of renewable electricity has fallen in recent years[1], the CO_2 electrolyzer technology has garnered significant interest as a strategy to reduce CO_2 emissions whilst producing value-added products because this technology operates under mild conditions (i.e., near room temperature and ambient pressure), has a modular cell design and relatively small system footprint, and provides a high degree of flexibility for use in carbon-intensive manufacturing processes (e.g., iron making, cement, and ammonia manufacturing). Substantial advances have been achieved in developing catalysts[2-8], electrode structures[9-11], membranes[12-15], reactor configurations[16-18], process design, and optimizations[19-27]. These collective efforts have enabled the CO_2 electrolyzer to operate close to commercially viable rates with good stability, and several pilot-scale electrolyzers[28-31] have been built.

The principal components of CO_2 electrolyzers are an anode, a cathode, and a membrane or separator, as shown in Figure 1a. The anode is where oxidation reactions take place, with the most common anode reaction being water oxidation (so-called oxygen evolution reaction, OER). Other anode reactions demonstrated with CO_2 electrolysis include chlorine evolution[32, 33] and oxidation of organic compounds that can be coupled with CO_2 electrolysis[34-36]. Some of these alternative reactions require lower overall cell voltages or produce value-added products and could potentially enhance the overall economic feasibility.[37] The water-permeable and ion-selective membrane allows transport of desired ions to complete the electric circuit but should prevent the crossover of electrons and products between the two electrodes. The CO_2 is reduced at the cathode, and here water may also be reduced through the generally unwanted hydrogen evolution reaction (HER). The product distribution from the CO_2RR highly depends on the catalyst at the cathode. Cathode catalysts are broadly classified into three groups based on the major products of the CO_2RR[38]: (a) catalysts based on Sn, Bi, In, Pb to produce formic acid; (b) catalysts based on Ag, Au, Zn, Ni, Co, Pd to produce CO; and (c) Cu-based catalyst to produce hydrocarbons such as alkanes and alcohols.

Electrolyzer configurations have developed from the H-type cell with planar foil type electrodes to continuous flow cells using gas-diffusion electrode (GDE) at the cathode and anode. The position of the electrodes and membrane could be varied to optimize multiple flows (liquids, gases, electrons and ions) in the electrolyzer and control the local chemical and physical environments close to the catalyst surface. If there is electrolyte flowing in between the cathode and membrane, the reactor could be called a liquid-fed electrolyzer; if there is no gap between the cathode and membrane, the electrolyzer can be grouped into vapor-fed electrolyzers.[29, 39-41] (Figure 1a and b). The liquid-fed electrolyzer has

been widely used in the CO_2RR studies, while the vapor-fed electrolyser is gaining more research interest because of its minimal ohmic loss as a result of the eliminated catholyte between the cathode and membrane.[23]

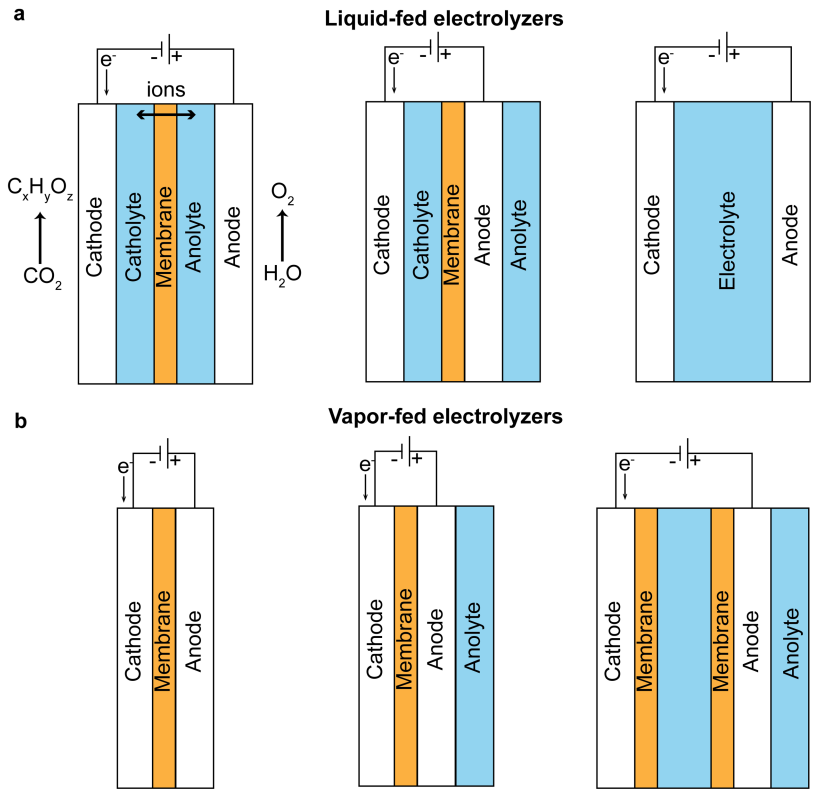

Figure 1 Schematic illustrations of (a) working principle of a typical liquid-fed CO_2 electrolyzer and other configurations, and (b) vapor-fed reactor configurations.

Gas-diffusion electrodes are emerging as an effective approach to increase the current densities by overcoming the gas diffusion limitations in the cathode. In fact, the most substantial improvements in CO_2 electrolyzer performance (cathode overpotential, selectivity, stability) in recent years have come from positioning a catalyst nearby a gas-liquid interface using GDE's.[42-44] However, engineering this gas-liquid interface is a complex problem because the location, surface area, and stability of this interface are affected by the wettability of the catalyst layer, use of ionomers and hydrophobic agents in the electrode preparation, and the porous texture and surface chemistry of the support material. In a typical carbon-based gas diffusion electrode, as shown in Figure 2a, CO_2 gas diffuses from the gas chamber to the catalyst layer (CL) through a porous medium, which is normally called a gas-diffusion layer (GDL). The GDL is often composed of a thick, porous layer with pore sizes in tens of microns (so-called macroporous layer) and a thin layer made by a mixture of carbon black and polytetrafluoroethylene (PTFE) with nano-sized pores (so-called microporous layer, MPL). The catalyst layer is positioned on top of the MPL facing the electrolyte or membrane. The CL includes the active catalyst materials for CO_2RR, ionomers that facilitate ion transport and catalyst immobilization, and

other additives such as PTFE and organic modifiers to tune the local catalyst environment. The CO_2 reactant can be fed to the catalyst layer by flowing by or through the GDE. (Figure 2b) The flow-by mode is widely used, while flow-through is recently gaining more attention, particularly for 3D-structured electrodes such as porous hollow fibers.[45-47] (Figure 2b) The catholyte in contact with the cathode provides a source of protons and a sink for the produced hydroxyl ions (OH^-) and CO_2RR liquid products. The electrolyte has a profound impact on the membrane hydration and CO_2RR performances (e.g., overpotentials and product distribution). [48-50]

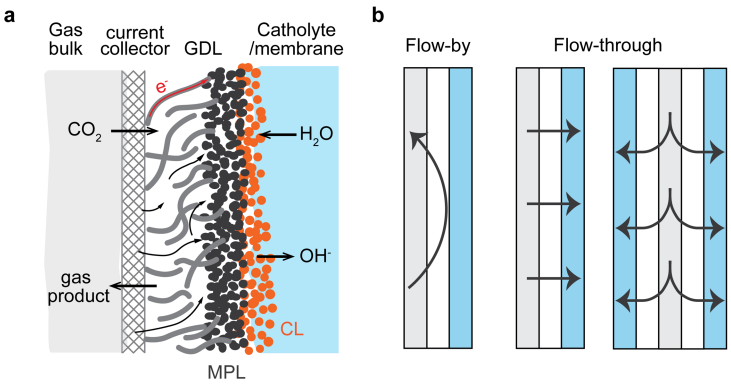

Figure 2 A schematic illustration of (a) a gas diffusion electrode structure and (b) common CO_2 gas flow patterns of the CO_2 feed in the cathode.

Despite the advancements provided by shifting gas-liquid interfaces in the systems for CO_2RR, it remains challenging to achieve a selective CO_2 conversion, particularly for long-term operation at high current densities. The primary challenges arise from the poor control of multiple flows (gas, liquid, and electrons) and local catalytic environment (e.g., pH, availability of water and CO_2) in the cathode structure throughout operation (e.g. from initial polarization to numerous hours of operation). For example, the CO_2 supply to the CL is often limited by high current densities (fast consumption of the CO_2 at catalyst surface) or highly alkaline electrolyte (loss of CO_2 due to carbonation). This CO_2 starvation could lead to the promotion of competitive HER.

Another critical issue of this technology is its long-term stability. At high current densities, the liquid electrolyte will usually imbibe or flood into the electrode pores over a short operating time. This flooding shifts the location of the gas-liquid interface over time, and because this interface is so critical to CO_2RR, the flooding changes the balance of reactants, ions, and water available at the catalyst sites. For example, pore invasion of the electrolyte increases the diffusion distance needed for CO_2, giving more time for the OH^- produced from CO_2RR and HER in the electrolyte to react with CO_2 to form carbonate or bicarbonate species. Electrolyte penetration into the GDL then further reduces CO_2 availability and causes a gradual cathode reaction shift from CO_2RR to HER. A subsequent issue related to flooding is that the solubility limits of carbonate and bicarbonate species such as K_2CO_3 (e.g., K_2CO_3

has a solubility of 8.03 mol kg^{-1} H_2O while $KHCO_3$ has a solubility of 3.62 mol kg^{-1} H_2O) are easily reached as water evaporates into the gas phase and ions quickly accumulate within the GDL's nanopores, which leads to salt precipitation.[51] Through a process similar to efflorescence[52], the crystallized salts are distributed discretely at the GDL surface likely because of (1) their screening effect that limits water evaporation to occur through the surface between isolated salt crystallites and (2) their porous and hygroscopic nature that pumps electrolyte through their structure via capillary forces. As a result, the precipitated salts (1) physically block the gas diffusion pathways in the electrode pores, (2) further consume CO_2 by reacting with carbonate deposits and moisture to form bicarbonates, and (3) accelerate electrolyte percolation. All of these further degrade the CO_2RR selectivity and long-term stability of the electrolyzers.[53, 54] If the wettability of the electrode could be tailored to avoid such challenges, as well as remain stable over the varied operation, vast improvements in stability and current density are possible.

In brief, there are still substantial opportunities to engineer the positioning of micro- and nano-interfaces to optimize the performance of CO_2 electrolyzers. This review sheds light on the work completed to date to improve performances of CO_2 electrolyzers through wettability modifications of the catalyst, ionomer, and support of the cathode. Figure 3 provides a high-level mind map of the materials covered in this review and potential opportunities to optimize electrode wettability in CO_2 electrolyzers. Here we do not discuss in detail the advances in understanding and developing anode and cathode catalysts, membranes, and electrolyzer structures because there are many comprehensive reviews on these topics available already[55-60]. Instead, we begin this review by discussing the desired wetting conditions of the GDL and CLs for CO_2RR based on the current understanding of the primary CO_2RR regions and recent achievement on CO_2RR performance via wettability adjustment. Then we review the recent advances in improving CO_2RR efficiency and selectivity by controlling the wettability of the catalyst surface, the CL, and GDL at a scale from micron- to nano- sizes. This review concludes with a discussion of future opportunities to design robust and high-performance CO_2RR electrodes in view of wettability optimization.

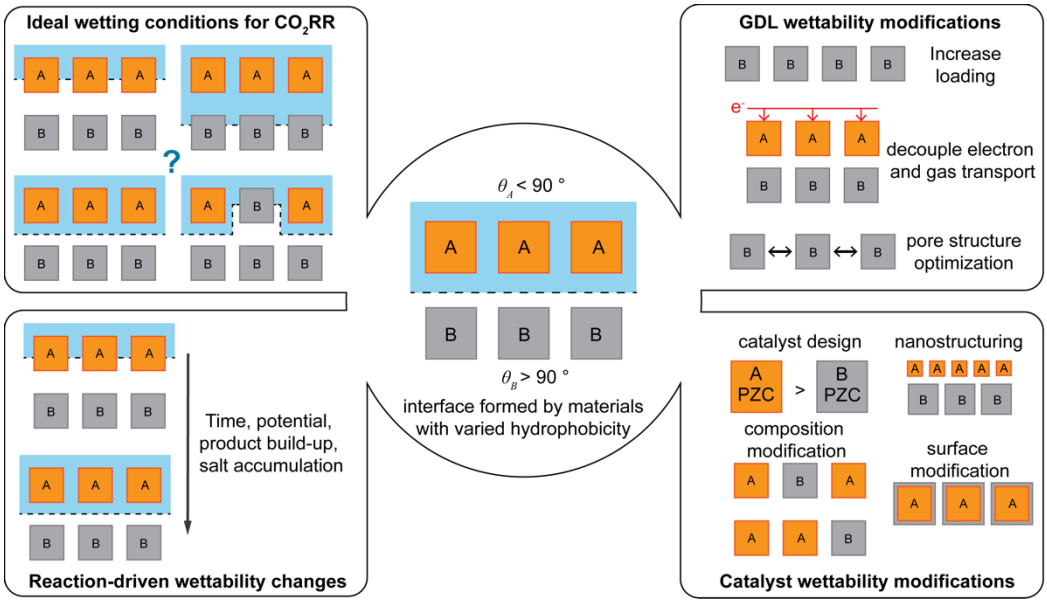

Figure 3 The role of the wettability in the electrode for CO_2RR and wettability modification methods to improve electrode performance. PZC is short for the potential of zero charges. The electrode can be considered as interfaces of materials with varied wettability. A represent hydrophilic materials such as catalyst and carbons in the electrode, and B represents hydrophobic materials such as PTFE.

2. Fundamentals of wetting

Wetting is the most basic interfacial interaction between solid and fluid. Whether a liquid can wet a solid surface is determined by intramolecular forces such as van der Waals and electrostatic forces (or Coulombic forces).[61] A strong intramolecular force, which is a nanoscale phenomenon, normally leads to a strengthened solid-liquid interaction and hence a reduction of the contact angle on a macro scale. The van der Waals forces develop at the solid-liquid interfaces and can be grouped into London dispersion, Debye, and Keesom forces based on the arrangement of the dipole interactions.[62] The London dispersion force is generally weaker than Debye (dipole-molecule) and Keesom (dipole-dipole) forces because it originates from random charge re-distribution in molecules with no permanent dipoles. All these forces are highly dependent on the chemical properties of the solid and liquid such as polarity, dipole moments, structures, and charging states. Besides, the porous structure (or heterogeneity) and chemical heterogeneity in the GDEs further add complexity to understanding wetting behavior.

2.1 Static wetting and capillary pressure

The classical approach to quantify the wettability of a solid is using the contact angle (θ) between the solid surface and a liquid droplet. (Figure 4a) If the liquid is water, when $\theta < 90°$, the surface is defined as hydrophilic while for $\theta > 90°$, the surface is defined as hydrophobic. When the droplet is at equilibrium over a surface that is flat and chemically homogeneous, θ can be calculated from the solid–vapor (SV), solid-liquid (SL), and liquid-vapor (LV) interfacial surface tensions (γ) according to Young's equation[63]:

$$\gamma_{SV} = \gamma_{SL} + \gamma_{LV} \cos\theta \qquad \text{Eq. 1}$$

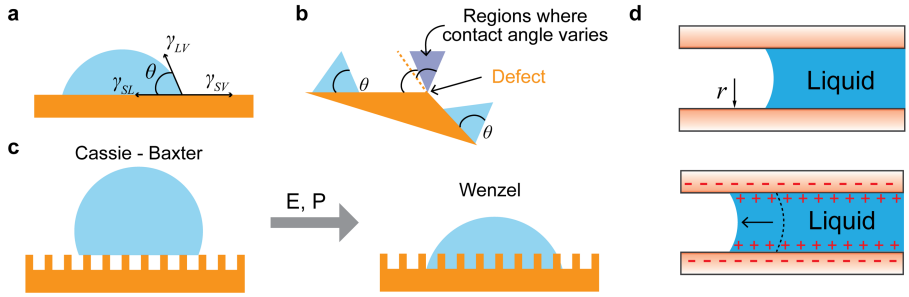

Figure 4 A schematic illustration of (a) static contact angle at an ideal flat surface and (b) at a surface with defect, where the contact angle varies. The defect could be either chemical defects (corners, kinks, dopant or vacancies) or microstructure defects (e.g., rough surface) (c) Cassie-Baxter and Wenzel wetting regimes, and electric field (denoted as E) and pressure (P) can initiate the transition from Cassie-Baxter to Wenzel states. (d) Schematic illustration of the static wetting states in the pore.

However, as real surfaces like the CO_2RR catalyst layers are not ideally flat, the wetting behavior varies significantly if the surface is rough or chemically heterogeneous. Chemical or microstructure defects can pin the water at the contact line and deviate the apparent contact angle significantly, as shown in purple regions highlighted in Figure 4b. Wenzel and Cassie-Baxter states are the two common wetting regimes of the droplet at rough surfaces. As shown in Figure 4c, in the Wenzel state, the droplet spreads until all the gas-solid interfaces underneath are replaced with the liquid-solid interfaces, while in Cassie – Baxter state, there are gas pockets trapped within the surface microstructure and below the droplet. The relations between the apparent contact angle and the intrinsic contact angle can be described by Eq. 2 for the Wenzel state and by Eq.3 for the Cassie-Baxter state. Note that these two models are only valid when the droplet is far larger than the surface microstructure so that the droplet wetting behavior can rely on the averaged properties of the solid surface.[64]

$$\cos\theta^* = R \times \cos\theta,\ R = \frac{area_{real}}{area_{geo}} \qquad \text{Eq. 2}$$

$$\cos\theta^* = f(\cos\theta + 1) - 1,\ \ f = \frac{area_{solid}}{area_{solid} + area_{air}} \qquad \text{Eq. 3}$$

Where θ^* is the apparent contact angle; R is the roughness factor of the rough surface; f is the fraction of the solid surface of the porous surface.

According to the Wenzel relation[65] as described by Eq.2, in general, an increase in the surface roughness will (a) increase wettability if the material is hydrophilic (b) but promote hydrophobicity if the material is hydrophobic. In the Cassie – Baxter state, the gas pockets are trapped in the structure if the following conditions are met: (1) the surface is chemically hydrophobic (Young's angle is larger than 90°) and (2) the surface is very rough.[66] When placing a droplet onto the surface with a moderate level of hydrophobicity and roughness (meaning that Wenzel is slightly more energetically favorable),

one could still observe a metastable Cassie – Baxter state until the liquid nucleates a contact with the solid surface. Such metastable Cassie – Baxter could transform to the Wenzel states if there is a perturbation such as pressure or electric field [67, 68] that overcomes the energy barrier required to wet the inner walls within the surface texture.[66]

In CO_2RR, the GDE is comprised of interfaces formed by materials with different wettabilities, as illustrated in Figure 3. The liquid phase typically includes electrolytes, liquid products and condensed water in vapor-fed electrolyzers. If considering the GDE as a porous medium containing a network of connected porous cylinders (Figure 4d), we could describe the capillary pressure P_c by using Eq. 4, as derived from the Young-Laplace equation, if the gas and liquid are in static conditions. The pores can be easily filled with the liquid (or high capillary pressure) if the liquid can easily wet the solid surface. However, this approach does not consider the effects of the electric field, which is present during CO_2RR. The effects of the electric field are discussed in the following section.

$$P_C = \frac{2 \times \gamma_{LV} \cos\theta}{r} = \frac{2 \times (\gamma_{SV} - \gamma_{SL})}{r} \qquad \text{Eq. 4}$$

Where P_C is the capillary pressure and *r represents* the radius of the pores shown in Figure 4d.[69]

2.2 Wetting under electric field

Under CO_2RR conditions, an electric double layer (EDL) structure will be formed at the solid-liquid interface under an electric field. The solvated cations are accumulated close to the electrode to neutralize the negatively charged interfaces. According to the Stern model, the electric double layer comprises of Stern layer and diffusive layer. The Stern layer contains the inner Helmholtz plane (IHP) for specifically adsorbed ions (ions with low hydration capacity) and the outer Helmholtz plane (OHP) for non-specifically adsorbed ions. The EDL thickness is about a few nanometers[70] and can be estimated using the Deybe length of the charged bulk electrolyte. However, the Deybe length approach may oversimplify the situation by ignoring some important characteristics such as intramolecular interaction, ion-ion correlations and excluded volumes.[71] The EDL thickness is expected to decrease in the electrolyte with concentrated ions, the high charge of the ions, and reduced ionic sizes.

Under an applied electrical field, the liquid generally becomes easily spread over the surface in CO_2RR conditions. This phenomenon is called electrowetting. Lippmann-Young's equation (see Eq. 5) describes the relations between the contact angle and the applied potential. [72]

$$\cos\theta_E = \cos\theta_0 + \frac{1}{2}\frac{\varepsilon\varepsilon_0}{\gamma_{LV} d}\left(E - E_{pzc}\right)^2 \qquad \text{Eq. 5}$$

Where θ_E is the contact angle under the applied electric field E; E_{pzc} is the potential of the zero charge; θ_0 is the contact angle in the absence of electric double layer; ε_0 is the permittivity of the free space; ε is the dielectric constant of the liquid on the electrically-conductive substrate or dielectric constant of the layer if the electrode is coated with the dielectric layer; d is the thickness of the double layer or the dielectric layer, and normally decreases with increasing ion concentration.

The electrowetting can take place at both electrically conductive materials such as carbons and metals and dielectric materials such as PTFE. The wettability is more sensitive to the electric field over conductive materials such as catalysts and the carbon blacks within the GDL than over dielectric materials. This general trend originates from: (1) generally higher dielectric constant of liquid phase (e.g., the dielectric constant of water ε_{water} = 80 at 20 °C) than that of dielectric materials (e.g., ε_{PTFE} = 2); (2) thinner thickness of the EDLs (typically < 50nm[70, 73]) than the dielectric PTFE coating on the conductive substrate. This means that the dielectric hydrophobic materials in the GDEs are more reluctant to lose their hydrophobicity under the electric field than electrically conductive metal- or carbon-based materials. In this case, the incorporation of dielectric hydrophobic materials in the CL could be helpful to maintain gas pathways and primary liquid-solid reaction zones. However, the electron-conductive materials in typical MPLs could promote wetting under the electric field and thus contribute to the commonly observed flooding issues.[53, 74-76]

This equation also indicates that the highest hydrophobicity can be achieved at the potential of zero charges (PZC), at which there is no excess charge at the solid-liquid interface. Deviating the electrode potential from the PZC will charge the EDL at the interface. The potential of zero charge is a basic property of the metal-solution interphase[77] and could vary with the surface facets, temperatures, and composition of the surface adsorbates. For example, Cu (111) and Cu (100) have the potential of PZC of -0.2 V and -0.54 V vs. standard hydrogen electrode (SHE), respectively. A summary of the common PZC values of the CO_2RR catalysts is provided in Table 1. The PZC can also be shifted by surface modification: negatively charged functional groups such as sulfonate shift the PZC towards a more positive value, while positively charged functional groups such as quaternary ammonium shift the PZC to a negative position.[78, 79] Recent modelling work highlighted the importance of the PZC in CO_2RR because it determines the effective electric field as the catalytic interface.[50, 80] Because a negative potential is required to drive the cathodic CO_2RR, a positive PZC makes the liquid easy to spread at the solid surface and also intensifies the interfacial electric field that drives CO_2 adsorption and the charge-transfer processes.[50]

Table 1 A summary of the potential of zero charge for CO_2RR catalysts.

Material	CO_2RR Products	Electrolyte for PZC test	PZC (V vs SHE)	References

pc-Pb	$HCOO^-$	NaF	-0.60 ± 0.02	81, 82
		Na_2SO_4	-0.60 ± 0.02	81, 82
		KF	-0.59 ± 0.01	83
		KNO_3	-0.59 ± 0.02	84
Pb (111)		NaF	-0.62 ± 0.01	81, 82
		Na_2SO_4	-0.62 ± 0.01	81, 82
Pb (100)		NaF	-0.62 ± 0.01	81, 82
		Na_2SO_4	-0.59 ± 0.01	81, 82
Pb (110)		NaF	-0.58 ± 0.01	81, 82
		Na_2SO_4	-0.58 ± 0.01	81, 82
Pb (112)		NaF	-0.58 ± 0.01	81, 82
		Na_2SO_4	-0.58 ± 0.01	81, 82
pc-Sn	$HCOO^-$	Na_2SO_4	-0.43	85
		K_2SO_4	-0.37 ± 0.02	86
		$KClO_4$	-0.39 ± 0.02	86
		Na_2SO_4	-0.39 ± 0.01	87
Sn (001)		Na_2SO_4	-0.37 ± 0.01	87
Sn (1-110)		Na_2SO_4	-0.37 ± 0.01	87
Sn (110)		Na_2SO_4	-0.38 ± 0.01	87
Bi (111)	$HCOO^-$	H_2O	-0.434 ± 0.005	88, 89
Bi (-10-1)		H_2O	-0.34 ± 0.01	88, 89
Bi (001)		H_2O	-0.35 ± 0.01	88, 89
Bi (01-1)		H_2O	-0.35 ± 0.01	88, 89
Bi (2-11)		H_2O	-0.33 ± 0.015	88, 89
pc-Ag	CO	NaF	-0.70 to -0.72	90
		$NaClO_4$	-0.744 ± 0.005	91
		$LiClO_4$	-0.69 ± 0.01	92
		Na_2SO_4	-0.678 ± 0.015	93, 94
			-0.703 ± 0.015	95
			-0.66 ± 0.02	96
Ag (111)		NaF	-0.454 ± 0.010	90, 97
		KF, NaF	-0.460 ± 0.002	98
Ag (100)		KF	-0.609 ± 0.002	98
		NaF	-0.621 ± 0.005	90, 99, 100
Ag (110)		$NaBF_4.LiClO_4$	-0.734 ± 0.005	101, 102
		NaF	-0.734 ± 0.005	103
Ag (311)		NaF	-0.664 ± 0.005	104
Ag (331)		NaF	-0.670 ± 0.010	104
Ag (210)		NaF	-0.750 ± 0.010	105
pc-Au	CO	NaF	0.20	102
Au (111)		NaF	0.56 ± 0.01	102
		H_2SO_4	0.56 ± 0.01	106-108
		$HClO_4$	0.55 ± 0.01	109
		$HClO_4$	0.47 ± 0.01	110
Au (100)		NaF	0.33 ± 0.01	111
		H_2SO_4	0.32 ± 0.01	106-108
		$HClO_4$	0.29 ± 0.01	110
Au (110)		NaF	0.19 +- 0.01	102
		$HClO_4$	0.19 ± 0.01	110
Au (210)		NaF	0.11 ± 0.01	102
Au (311)		NaF	0.25 ± 0.01	102
pc-Zn	CO	$NaClO_4$	-0.92	112
		KCl	-0.91	113
Zn (0001)		$NaClO_4$	-0.90 ± 0.01	114, 115
Zn (10-10)		NaF + camphor	-0.85 ± 0.02	114, 115
Zn (11-20)		NaF + camphor	-0.87 ± 0.02	114, 115
pc-Cu	C_2H_4	NaF	0.09	116
		NaF	0.50	117
Cu (111)	CH_4	NaF	-0.01	118
		$KClO_4$	-0.20 ± 0.01	119

Cu (100)	C_2H_4	NaF	-0.04	118
		$KClO_4$	-0.54 ± 0.01	119
Cu (110)	C_2 product	NaF	-0.071	118
		$NaClO_4$	-0.69 ± 0.01	119
Graphite	N/A	KF	-0.125	120
		KCl	-0.175	120
		KBr	-0.220	120
Carbon nanotube		NaCl	0	79
Single graphene nanoplatelets		KCl	-0.14 ± 0.003	121
Activated carbon		NaCl	0.605 (V vs Ag/AgCl)	78

The liquid surface tension used in Eq.5 is mainly used to estimate the contact angle under a certain electric field. With the surface tension removed, the second term constitutes the electrochemical capillary pressure (ECP), as described in Eq. 6, generated in a microchannel with length *l* and channel cross-area (*A*) to move the liquid.[122] Jones [123] argued that this term describes the electromechanical force due to the non-uniformity of the electric field because this term is independent of the contact angle or meniscus shape and can also be derived from lumped parameter model or Maxwell stress tensor. Therefore, the electrochemical capillary pressure generated within the CLs and MPLs could be one of the driving forces for electrolyte penetration. Similarly, we expect the liquid tends to wet pores with electrically conductive surfaces than those constructed by dielectric materials. Instead, the reduction of the intrinsic contact angle under the electric field is a result of the re-distribution of the charges at the interface and change of the interface tensions[124] and could be another driver for the increase of the electrode wettability at CO_2RR conditions.

$$\mathrm{ECP} = \frac{1}{A}\frac{\varepsilon\varepsilon_0}{d}\left(E - E_{pzc}\right)^2 \qquad \text{Eq. 6}$$

Additionally, the electric field could induce changes in both the liquid and solid phases. In the liquid phase, it is well known that pH, cations, anions and liquid behavior can vary significantly under CO_2RR conditions, and these liquid properties can impact the wetting of the catalyst layer. Section 3.1 provides a detailed discussion of the effects of liquid properties such as pH and ion types on the electrode wetting conditions. Additionally, an electric field can effect surface chemistry [125, 126] and morphology [127-132] of the solid phase, which will impact wetting conditions. Yang et al.'s [75] reported such effects observed in experiments with X-ray photoelectron spectra to detect the loss of C-F bonds and increase in the concentration of oxygen species at the GDL surface after exposure to cathodic conditions, and this effect may explain the loss of the wettability in the CLs. These recent observations are consistent with Shapoval et al.'s reports from the mid-1980s on the degradation of PTFE under cathodic conditioning.[133] In Section 3.2, we discuss in more detail the possible impacts of the electric field on the solid phase.

The total charge passed during CO_2RR could also play a role in electrolyte seepage in the electrode structure. Leonard et al.[53] reported a single sigmoidal curve relation between the accumulated charge and the electrode wetting (reflected by the degradation of CO mole fraction in the gas phase or increase of the EDL capacitance). (Figure 5a and b) The trend is similar to the water saturation – Leverett J-function (i.e., a function describing the capillary pressure, liquid tension, porosity, and permeability) in GDLs used for PEM fuel cell electrodes.[134] (Figure 5c) The non-wetting phase saturation indicates the ratio of the volumes of non-wetted pores to the total pore volumes. The GDL substrate normally contains most of the pore volumes due to its significant thickness and large pores (usually in micro size). When the electrolyte invades and occupies the pores in the GDL, it will block the gas transport significantly and leads to the observed degradation of the CO selectivity in Leonard et al.'s experiment.[53] In this case, the decrease in the non-wetting phase saturation becomes noticeable, like the case shown in Figure 5c. Their similarity highlights the potential link between the CO product selectivity and the pore saturation conditions in the GDE, where the accumulated charge plays an essential role.

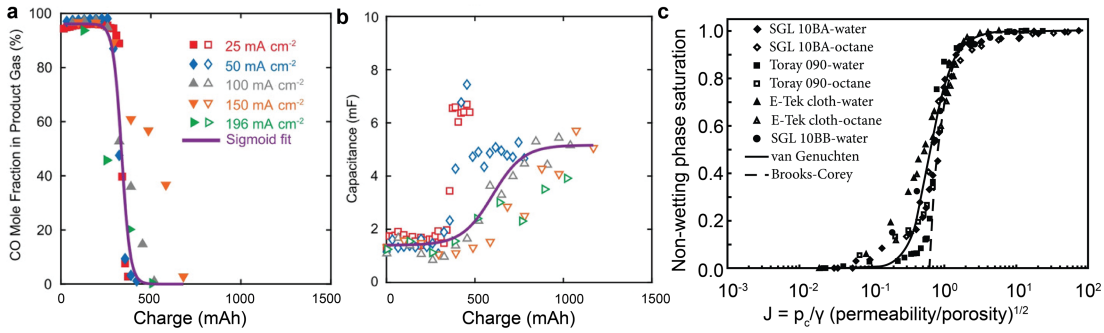

Figure 5 The relationship of (a) CO product mole fraction in product gas and (b) measured capacitance of the electrode with the total charge during CO_2RR. Reproduced from [53] with permission from John Wiley and Son, copyright 2019. (c) Leverett J-function correlation with the non-wetting phase saturation over different GDLs with water or octane, and the simulated results based on van Genuchten and Brooks-Corey models. Reproduced from [134] with permission from Elsevier, copyright 2006.

2.3 Efflorescence at CO_2RR gas-diffusion cathode

As discussed in the introduction, the OH^- ions produced by the cathode reactions tend to react CO_2 to form less soluble salts such as carbonates, which usually precipitate as efflorescences in the electrodes at a high local pH (e.g., high current densities, alkaline electrolytes or anion exchange membrane-based MEA with limited water). [22, 53, 54] The salts are normally porous and hydrophilic and hence increase the capillary pressure that accelerates electrolyte flooding in the electrode by drawing water into the GDE pores. The ion types and concentration of the electrolyte play a role in determining the nucleation and growth of the efflorescence. For example, Cofell et al.[54] reported that CsOH-based electrolyte leads to the formation of small and well-dispersed crystals electrode at the electrode surface, while KOH-based electrolytes render large and segregated precipitates at CO_2RR conditioning at 200 mA cm^{-2} over Ag-based GDEs. The authors believed that the observed trend mainly results from

the solubility of the salts and the hydration of the cations. It is as expected that salts with a lower solubility (e.g., $KHCO_3$ has a lower solubility than $CsHCO_3$) will nucleate when their local concentrations exceed their solubility limits. A high ionic concentration of the electrolyte increases the surface coverage and sizes of the precipitated crystals. In addition, strongly hydrated cations (e.g., small and highly charged cations) are difficult to remove water molecules from their hydration shell, slowing the nucleation process and thus resulting in discrete and large crystals. The authors also reported a significant salt precipitation related degradation of the CO selectivity at high current densities, i.e., the electrode with small salt deposits has a less negative impact on CO_2RR selectivity than the one with large salt deposits.

2.4 Desired wetting conditions for CO_2RR gas-diffusion cathodes

Within a typical GDE, the pore structure of the GDL (including macroporous layer and MPL) is designed to be gas wet to allow fast diffusion of CO_2 to CL and gaseous product to the gas bulk. Conversely, the CL should be wet or partially wet by the electrolyte, which serves as the source of protons and sinks for liquid products such as hydroxide ions, formate, and alcohols.[9, 49] However, the current understanding or description of the ideal catalyst wetting conditions still remains ambiguous.

One popular description of the desired CL wetting state is the CL structure with many gas – liquid – solid triple phase boundaries (TPBs). This description originates from (1) the fact that CO_2RR requires the CO_2 and protons as reactants and a sink for liquid products and (2) the common observation of enhanced CO_2RR reactivity and selectivity over CLs with a moderate increase of hydrophobicity.[126-130] For example, Shi et al.[137] argued that the co-existence of Wenzel state and Cassie-Baxter states (i.e., moderately hydrophobic CLs) are ideal wetting conditions for CO_2RR to produce CO. Their conclusions are mainly based on the correlation between CO_2RR performance, and ex-situ confocal laser scanning microscopy (CLSM) results over Au/carbon black-based CLs with various wetting states, which were achieved by treating the carbon black with fluorinated silane (Au/C-F) or air plasma at various durations (Au/C-P-0.5 and Au/C-P-2.5). (Figure 6) They confirmed from the CLSM results that the CL hydrophobicity decreases in the order Au/C-F (Cassie-Baxter) > Au/C-P-0.5 (co-existence of both states) > Au/C-P-2.5 (Wenzel) (Figure 6d-1f), and from the CO_2RR tests that Au/C-P-0.5 shows superior performance than the rest two analogs. Note that the samples Shi et al. used for CLSM characterization were prepared by pressing the CLs onto a droplet of 1M KOH aqueous solution labelled with fluorescein, which cannot truly reflect the wetting conditions under a cathodic potential. Nevertheless, this work is a step forward in understanding the ideal wetting conditions of CL for CO_2RR experimentally.

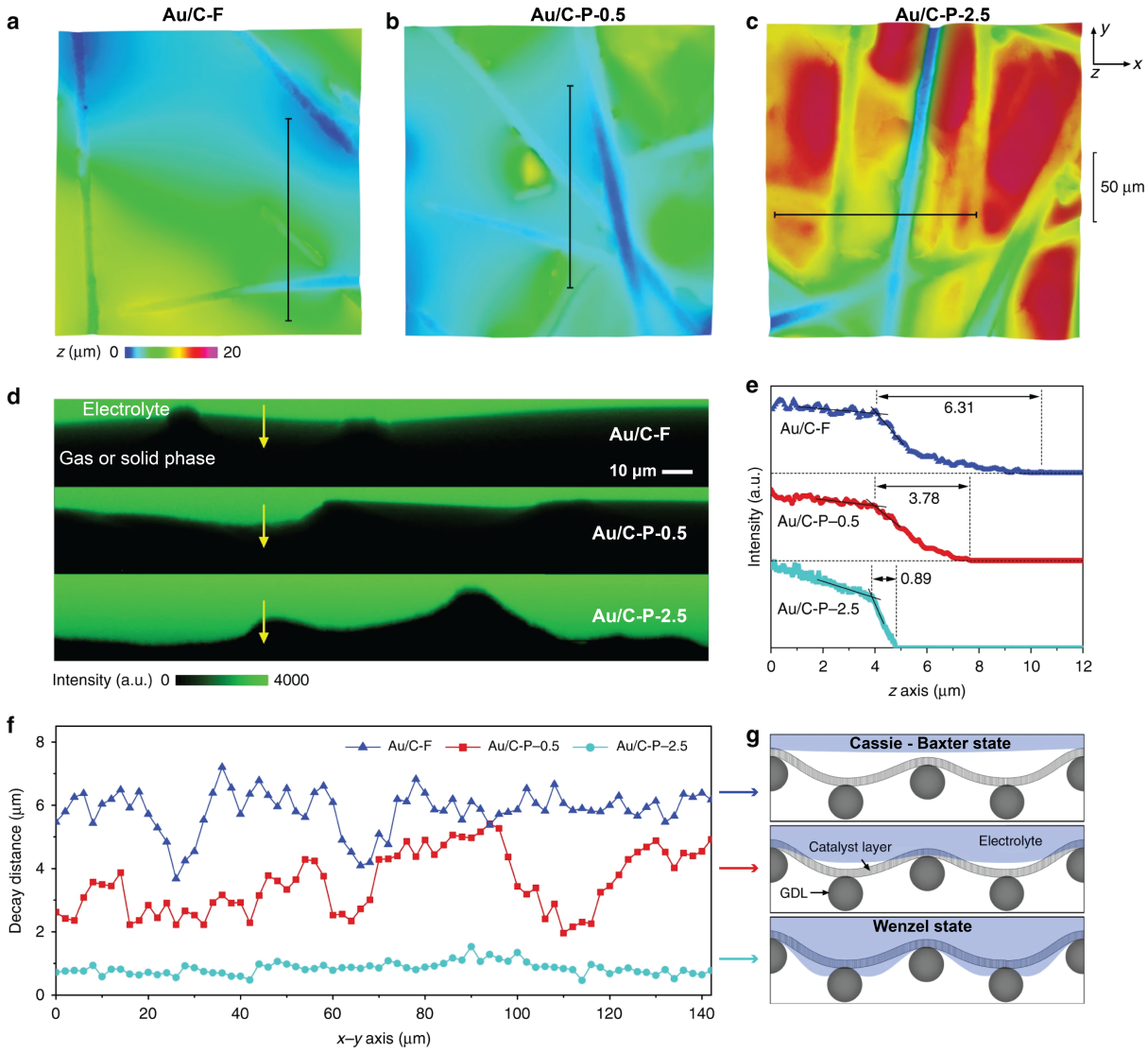

Figure 6 Confocal laser scanning microscopy 3D reconstructed images for (a) Au/C-F, (b) Au/C-P-0.5 and (c) Au/C-P-2.5. (d) Cross-sections of fluorescence images of the regions of (a-c) labelled by the black lines. (e) the fluorescence intensity profile as a function of z-direction at the regions labelled with yellow arrows in cross-areas shown in (d). (f) Statistics of the fluoresce decay distance from the entire region of the image (d). (g) Schematic illustration of the wetting conditions of Au/C-F, Au/C-P-0.5, and Au/C-P-2.5. Au/C-F are Au and carbon black treated with fluorinated silane, and Au/C-P-x denote Au/carbon black that is treated with air plasma for x min. Reproduced from [137] with permission from Springer Nature, copyright 2020.

Nevertheless, the triple-phase boundaries' role in CO_2RR or even the TPB locations in the GDEs (*i.e.*, either within the CL or at the CL – GDL interfaces) are not explicitly described. If the triple-phase boundary is the primary reaction zone, as shown in Figure 7a, the CO_2RR should involve CO_2 adsorption at dry catalyst surface and migration of either adsorbed CO_2 species at gas-solid interfaces or hydride ions from the liquid-solid interfaces. However, these two steps are not energetically favorable because (1) the CO_2 adsorption at the dry metal surface is weak (e.g., it requires a pressure of 33 atm to allow CO_2 adsorbs at Cu(111) at 25 °C) [140], and (2) the CO_2 diffusivity along the dry surface (a level of 10^{-8} $cm^2\ s^{-1}$)[43] is much slower than through the liquid phase (at a level of 10^{-5} $cm^2\ s^{-1}$).[43, 132] Despite a faster CO_2 diffusion in the CO_2 film (i.e., the interphase between CO_2 gas and water, denoted by the grey

color region at the gas-liquid interface in Figure 7a), the contact between the film (only about 0.5 nm thick) and catalyst surface is too limited to serve as the primary reaction regions.[43] Further critical discussion of the dominant phase boundaries within a uniform porous catalyst layer for CO_2RR can be found in the recent perspective by Nesbitt et al.[43], who critically reviewed the dominant phase boundaries within a uniform porous catalyst layer for CO_2RR. The key conclusions drawn by Nesbitt et al. include: (1) the CL pores should be filled with liquid under CO_2RR conditions (Figure 7b); (2) the liquid–catalyst interfaces within the CLs are the dominant reaction regions in an atomistic scale; (3) the reaction zone was expected to be 10 – 1000 nm in size extending from the catalyst surface to ensure sufficient CO_2, water supply and fast OH^- migration. These conclusions are consistent with the statements of the earlier work by Weng et al.[42]and Burdyny and Wilson[44] (co-authors of Nesbitt et al.'s perspective).

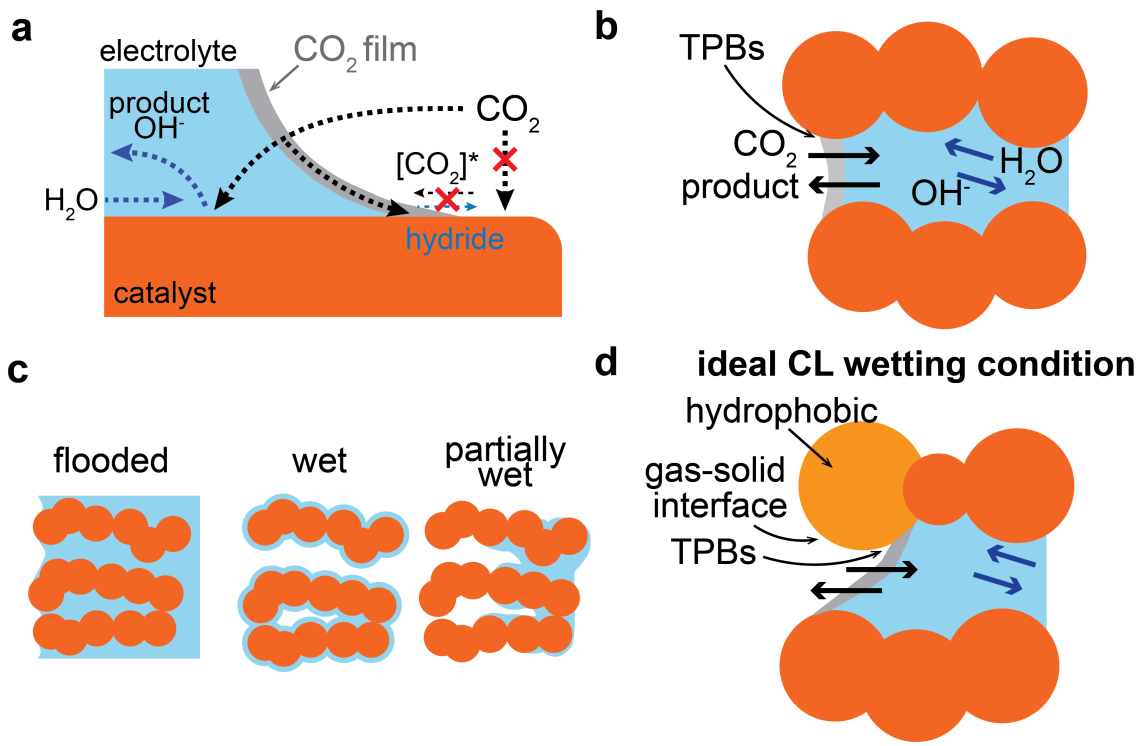

Figure 7 Schematic illustration of (a) potential pathways for CO_2 transport to the catalyst surface at TPBs, (b) possible wetting conditions at the pores of the homogenous CL, (c) potential wetting conditions in the CL structure, and (d) the desired wetting conditions for the CL pore. (a) and (b) are reproduced from [43] with permission from American Chemical Society, copyright 2020, (c) is reproduced from [43] with permission from American Chemical Society, copyright 2020, and (d) is adapted from [42] with permission from The Royal Society of Chemistry, copyright 2020.

Additionally, Weng et al.[42] pointed out that the CO_2 concentration is not significantly higher in the gas phase (42 mM at 20 °C and 1 atm) than in water (33 mM), which cannot explain the significant improvement of reaction rates by at least an order of magnitude over GDEs than over planar electrode immersed in an electrolyte.[74, 133] Instead, this enhancement over GDE can be considered to be a result of (1) the shortened CO_2 diffusion distances in the liquid film from 40 – 160 µm [134, 135] to 0.01 – 20 µm

[42, 136] and (2) an increased density of active sites per geometric electrode area. Again, note that the relatively thick hydrodynamic layers (0.01 – 20 μm) at the catalyst surface makes the CL pores (typically less than a few hundred nanometers in size) [137-140] hardly maintain a wet pore condition (i.e., the pore surface is wet while gas still transports through, as depicted in Figure 7c) as proposed by Weng et al.[42]. This statement is particularly true if there are no hydrophobic additives such as PTFE in the CLs or a high capillary pressure to enable the gas to displace the filled liquid within the CL pores.[43] If the catalyst pores are filled with electrolyte, the TPBs should be limited at the CL – GDL adjunctions. Hence changing CL thickness is expected to have minimal impacts on the CO_2RR activity if TPBs are the main reaction regions in CLs. However, it is contradictory to CO_2RR results obtained by Wu et al.[147], Dinh et al.[74], and Qi et al.[149], where changes to catalyst layer thickness show an impact on CO_2RR performance, meaning that TPBs cannot be the primary reaction regions for CO_2RR.

Presuming the primary reaction zone is located at the liquid-solid interfaces as discussed by Nesbitt et al.[43], we could consider a revised explanation for the reported enhancement of CO_2RR activities over reports which utilize the moderately hydrophobic CLs[128, 142, 143], effectively creating a 'wet' and 'partially wet' scenarios illustrated in Figure 7c. The enhanced activity over GDEs is likely related to (1) the shortened diffusion length for CO_2 in the liquid phase to reach catalyst surface near the bulk electrolyte and (2) the extended gas-solid interfaces and TPBs across the CL structure, as illustrated in Figure 7d. Here the solid phase of the extended gas-solid interfaces and TPBs are non-reactive additives such as PTFE and carbon materials, rather than the catalytically active phases as we mentioned for the homogeneous CLs that are only made of catalyst materials. These gas-solid interfaces and TPBs embedded within the catalyst layer could provide gas-wet pathways for gaseous CO_2 and products transport. Meanwhile, the liquid-wet pathways within the CL could provide access for the electrolyte and CO_2RR liquid products (e.g., OH^- and formate ions) to migrate between CL and bulk electrolyte by crossing the locally distributed catalyst-liquid reaction zones. These gas-wet pathways within the CL can be constructed by incorporating hydrophobic additives such as alkaethiol[135] and PTFE particles[136, 142] in between the catalyst sites in the CLs. The liquid-wet pathways can be created at catalyst pores or by using hydrophilic additives such as air-plasma-treated carbon black[137] and ionomers[152]. The pathways made from non-reactive additives have minimal impacts on the density of the active sites as long as the catalyst sites are electrically conductive to the electrode and easily accessed by the bulk electrolyte. This CL configuration could also shorten the transport length for the dissolved CO_2 to the catalyst surface, particularly because it prevents the CO_2 migration in the liquid phase along the long pore to reach catalyst surfaces near the bulk electrolyte. Our new explanation could justify the essential role of the co-existence of Cassie-Baxter and Wenzel states

(Figure 6), as proposed by Shi et al. [137], within CL structure to promote CO_2RR performance. These should be the optimal wetting conditions of the electrode for both flow-through and flow-by modes.

We acknowledge the important role of the electron conductivity to determine the density of the electrochemically active sites for CO_2RR within the CL structure. The electron-conducting phases, such as carbon materials, are easily liquid wet under the electric field and therefore provide solid-liquid boundaries and transport pathways for electrolyte and liquid products. In contrast, the hydrophobic additives are not electrically conductive and could increase the overall ohmic loss of the electrode and lead to loss of the active sites if blocking the pathways for electron and liquid transport. [145, 146] Therefore, trade-offs exist between the multiple flows and the availability of the active sites in the CLs. These trade-offs are usually responsible for the observations that a moderate level of hydrophobicity is usually optimal for CO_2RR.[127, 136, 145]

In summary, we envisage the ideal wetting conditions at the CL should allow fast liquid and electron transport, maximize CO_2RR-active and selective sites and optimize catalyst local environments to thereby achieve a CO_2RR with low overpotential and high product selectivity and stability at commercially relevant current densities. This means that the electrode structure should be precisely constructed with a combination of the materials with different wettability and functionality, and provide multiple transport pathways to maintain a sufficient supply of gaseous CO_2, protons, and electron, and shortened travel distances of CO_2, electrolyte, and products (i.e., OH^- and CO_2RR products) in the liquid phase. Further, the density of electrochemically active sites should be maximized, which is an additional challenging constraint on such systems. Finally, the GDL should maintain a hydrophobic condition during varied CO_2RR operation to ensure a fast gas transport between the CL and gas bulk phase.

3. Improving CO_2RR performance by manipulating wettability

The previous section described wetting within CO_2RR in a holistic sense, describing the fundamental factors that influence wetting within the system and postulating on the ideal conditions required to maximum current density, stability, and general performance. Within this section, we provide an in-depth review of the role of the liquid and solid phases on electrode wettability and the modifications to wettability that have been employed in literature to modify electrochemical performance. Specifically, we discuss GDL, ionomers, catalysts, PTFE and other additives in detail, using examples to provide context to the discussion.

3.1 The role of liquid in electrode wettability

The ability for the liquid to wet a given surface is related to the cohesive forces between its molecules and the adhesive forces to a given solid phase. The cohesive force describes the intramolecular forces

to hold the liquid molecules in bulk; the adhesive forces are the attractive forces between the liquid and solid surface. If the adhesive force is stronger than the cohesive force, the liquid tends to spread at the solid surface, being more attracted to the solid phase. Normally, reducing liquid surface tension leads to a good wetting of the surface as the cohesive forces of the liquid are decreased.

Both cohesive and adhesive intramolecular forces are dependent on the properties of the liquids, such as polarity, ionic nature (e.g., size, electronegativity, and charge), ionic strength, and composition of the liquid phase. For example, Leonard et al.[155] compared the contact angles of the droplets based on CO_2RR liquid products (formic acid, methanol, ethanol, and 1-propanal) and their aqueous solutions over PTFE and graphite sheets. They found that the solutions containing a high concentration of CO_2RR liquid products are easier to spread at the surface than water, and their wetting capability increases with the length of carbon chains within the liquid. As a result, the contact angles of the liquid droplets on the graphite and PTFE generally increase in the order 1-propanol < ethanol < methanol < formic acid < water. (Figure 8) An increase of carbon chains reduces the polarity of the solvent and therefore leads to a weakened dipole-dipole cohesive interaction and an easy liquid spread at the surface. Their physical modelling results unveiled that producing concentrated liquid products with low polarity can cause flooding in the electrode and disrupt the operation of the electrolyzer. Their results highlight the importance of considering electrode wettability when designing a CO_2 electrolyzer to produce liquid products.

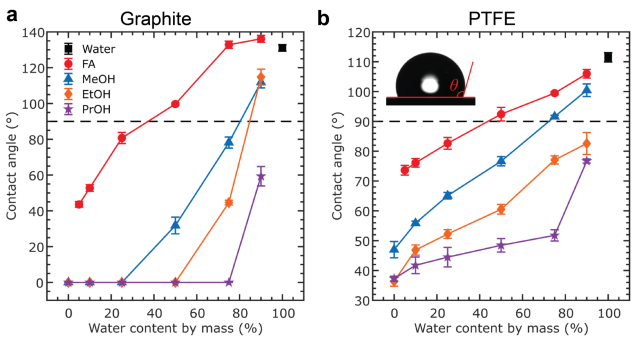

Figure 8 Comparison of the static contact angle of water and aqueous solutions containing liquid CO_2RR products on (a) graphite and (b) PTFE plates. Reproduced from [155] with permission from IOP Publishing, copyright 2020.

The effects of the ions on overall wettability are mainly related to hydration (ion-water interaction) and ion-solid interactions. Figure 9a presents a linear relation between cationic entropy of hydration and the gradient of the electrolyte surface tension ($d\Delta\gamma_{LV}/dc$) over metal chloride concentration.[156] Highly charged cations in small size are easily hydrated with water molecules, so increasing the concentration of such cations strengthens the cohesive forces and thus increases the solution surface tension. The cations with larger hydration size, such as Li^+ and Na^+, repel each other due to the thick hydration shell at the electrode surface, leading to a reduced cation concentration at the outer

Helmholtz plane.[50] Therefore, less hydrated cations such as K^+ and Cs^+ intensify the interfacial electric field by filling more cations in the EDL, which drives local CO_2 adsorption and promotes CO_2RR reactivity. Therefore, we conclude that the cations that enhance CO_2RR performance will lower the liquid tension and render the liquid easily spread at the surface.

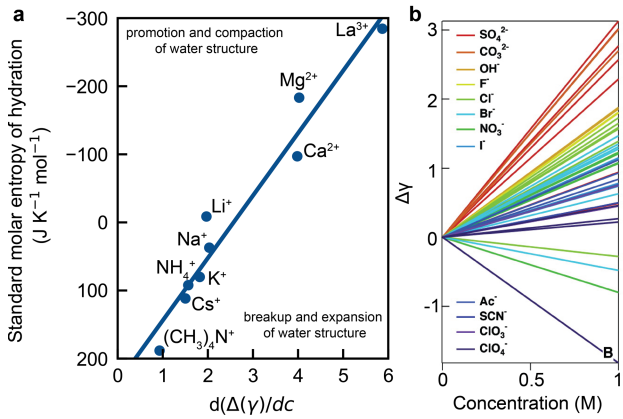

Figure 9 (a) Relationship between tension gradient of salt concentration and the entropies of hydration of cations. Adapted from [156] with permission from American Chemical Society, copyright 1995. (b) Effects of anion concentration on the change of the electrolyte surface tension. Adapted from [157] with permission from American Chemical Society, copyright 2007.

Similarly, solutions with concentrated hydrated anions (e.g., Cl^- is easier to be hydrated than Br^- and I^-) also increase the electrolyte surface tension by strengthening the cohesive interactions in solutions. (Figure 9b)[158] Upon interaction with the solid electrode, the anions with low hydration such as I^- tend to form a bond with the electrode surface in the inner Helmholtz plane (so-called specifically adsorbed) even at cathodic CO_2RR conditions.[150-153] Such strong anion interaction with the catalyst surface increases the adhesive force and promotes wetting of the solutions. The specific adsorption of anions at catalyst surface has a profound impact on the CO_2RR activity and selectivity by altering the surface morphology (e.g., nano-structuring the catalyst surface[151, 154]) and electronic structure and surface coverage of the intermediates (either stabilizing CO_2RR intermediates such as *COOH [159] or lower CO coverage [163])

Anion interaction with the hydrophobic surface also promotes the wetting of the liquid. In the absence of the external potential, OH^- ions tend to adsorb physically at the hydrophobic surface (e.g., PTFE) due to the interaction between permanent dipole moment of OH^- and electric potential gradient of the structured water (about two layers of water thick) close to the hydrophobic surface.[164] The spontaneous OH^- physisorption is reflected by a negative zeta potential over the PTFE surface.[165] This phenomenon could explain the observed reduced contact angle over the PTFE surface for liquids with a high pH.[166] In the presence of applied cathodic potential, we believe the anion interaction with the electrode surface should be weakened due to the electrostatic repulsion.

3.2 The role of solid phase in electrode wettability

The CO_2RR cathode GDEs are composed of functional materials with varied wettability, including catalyst materials (usually based on metals), organic additives such as PTFE and ionomers, polymers, and carbon materials (e.g., carbon black or fibers). These materials are placed together to maintain the multiphase interfaces and pathways and provide active sites for selective CO_2RR. However, their properties usually change with operating conditions (e.g., applied potential) and operating durations, particularly at commercially relevant current densities, which degrades the long-term stability of the electrolyzers.

Metal-based materials

Most clean metal surfaces are intrinsically hydrophilic as a result of the London dispersion forces.[159, 160] Oxygen incorporation at the metal surfaces further enhances the solid-liquid interfacial forces via hydrogen bond formation (i.e., a dipole-dipole interaction) with the water adlayers. Under non-ideal conditions, oxygen vacancies (i.e., defects) are usually present at the metal oxide surfaces and can further vary the wettability via influencing the solid-liquid intramolecular forces. The extent of their impact on wettability depends upon the materials' defect chemistry. Sarkar et al.[169] reported a lowered water contact angle over $SrTiO_3$ thin film but an increase of water contact angle over Lu_2O_3 thin film when oxygen vacancies were introduced. The oxygen vacancies are created by the reduction of Ti^{4+} to Ti^{3+} in $SrTiO_3$ but by defect formation in the bandgap in Lu_2O_3. Through DFT calculations, the authors found that it is energy favorable for water to insert into the oxygen vacancies at $SrTiO_3$ surface to maintain the Ti^{3+} states rather than into the metal site close to vacancies at the Lu_2O_3 surface. Therefore, the former strengthens the water–solid interactions and improves the water wettability.

This effect explains the much lower contact angles, as reported by our recent work[126], over 2D catalyst-based CL than over 3D catalyst-based CL. We prepared tin oxide-derived nanosheets (2D) and nanoparticles (3D) as CO_2RR catalysts deposited on GDE with similar particle sizes at around 100 nm, crystal structures, and oxidation states. After conditioned under CO_2RR conditions at 150 mA cm^{-2} for 60 min, the nanosheets were more chemically reduced at the surface (i.e., more oxygen vacancies, Figure 10a) due to the extensive catalyst–support contact (Figure 10b), as compared with nanoparticle-based counterpart. According to Sarkar et al.'s theory,[169] more water could insert into the oxygen vacancies over SnOx nanosheets than the nanoparticles, leading to a much-reduced water contact angle over SnOx nanosheets (Figure 10c). Consequently, we observed about 0.1 V more cathodic potential for the nanosheet-based GDEs to drive similar current densities, which is likely due to the hampered CO_2 supply in the CL. Additionally, Rabiee et al.'s recent work on hollow fiber-based GDEs also reported that the water could spread easily over the oxide-derived Bi nanosheets due to their abundant defects at the surface.[46] In this flow-through electrode, enhancing catalyst

hydrophilicity is more desired to maintain sufficient solid-liquid boundaries than the flow-by GDEs. In addition, the 2D nanostructured catalysts have also been used to achieve superaerophobicity to accelerate bubble detachment.[162-164] Therefore, the 2D morphology also partially contributes to the enhanced hydrophilicity over SnOx or BiOx nanosheets at CO_2RR conditions. Although the wetting states are very complex over CL surfaces that are generally heterogeneous chemically and in microstructure, these recent findings highlight the important roles of the catalyst materials in determining electrode wettability.

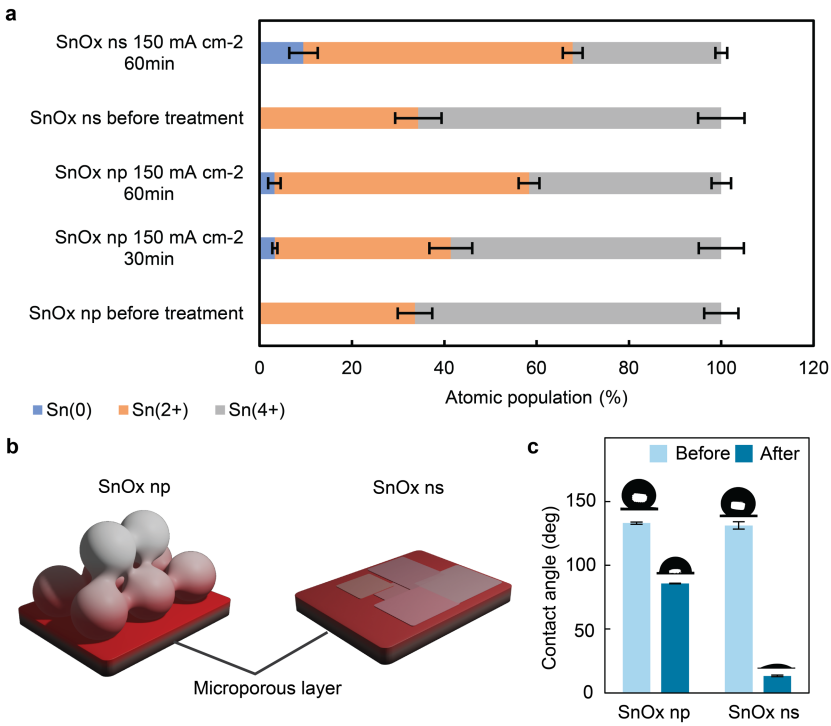

Figure 10 (a) Atomic populations of the Sn^0, Sn^{2+}, and Sn^{4+} at the surfaces of catalyst layer based on SnOx nanoparticles (np) and SnOx nanosheets (ns) before and after CO_2RR conditioning. (b) A schematic explanation of the effects of catalyst dimensionality on catalyst-substrate interfacial interactions. The red color describes the electric field profiles. (c) Static contact angles on catalyst layers before and after CO_2RR catalysis at 150 mA cm^{-2} for 60 min. The insets are examples of the water droplets on the catalyst layer. Reproduced from [126] with permission from The Royal Society of Chemistry, copyright 2021.

Beyond metals or oxide-derived materials, emerging catalysts contain metal centers and non-polar non-metal ligands, such as metal-organic frameworks and single-atom catalysts [3, 6, 8, 165, 166]. These materials become hydrophilic if the metal coordination environments are unsaturated.[3, 167] The coordinatively unsaturated metal centers are usually the primary active sites for CO_2RR because of their strong binding with intermediates.[168-171] As discussed in Section 2.4, the liquid–catalyst interfaces are the primary CO_2RR domains, so hydrophilicity is favored over the metal-based materials, which constitute most of the state-of-art CO_2RR catalysts.

Carbon-based materials

Carbon materials such as carbon fibers, carbon black, and carbon nanotubes are generally more hydrophobic than metals.[160, 172] Their wettability strongly depends on their structures and heterogenous atoms at the carbon surface.[181] Carbon black has graphene edges at the surface, constituting high-energy interaction sites with strengthened London dispersion force. Carbon nanotubes and graphene are more hydrophobic than carbon black due to the lack of high-energy defects at the surface. The heterogenous atoms (e.g., oxygen) at carbon surface, from either surface contamination or functional groups, can form polar sites that lead to strong dipole-dipole interactions and enhanced hydrophilicity. This effect has been widely exemplified by the enhanced hydrophilicity for carbon surfaces with a high oxygen coverage.[127, 173]

Organic additives – binders and ionomers

Fluorinated polymers such as PTFE[74, 76, 174, 175] and fluorinated silane[137] are the most commonly used materials to increase the hydrophobicity of GDLs and CLs because of their high hydrophobicity and chemical stability. Its high hydrophobicity originates from the fluorine's low polarizability and low London dispersion force, and its high chemical stability arises from fluorine's high electronegativity that makes C – F bonds strong. Polymers with long non-polar hydrocarbon chains, such as 1-octadecanethiol[184], are also hydrophobic.

The ionic functional groups (-SO_3 or quaternary ammonium) in the ionomers (e.g., Nafion or Sustainion) have high polarity and can take up water to form hydrophilic domains inside the polymer. As a result, the ionomers are hydrophobic if they are dry but can promote hydrophilicity when absorbing water at CO_2RR conditions.[144, 177] Puring et al.[146] studied the ionomer effects on the CL wettability by coating the CL with Nafion D-521, Sustainion XA-9, and Fumion FAA-3 ionomers at the same loading. The CL comprised carbon black-supported Cu nanoparticles (50 wt% metal loading) and 15 wt% of PTFE and was prepared by hot pressing. They reported that the apparent contact angle lowers in the order D-521 > FAA-3 > XA-9, but the water adsorption increases following the opposite order, though both high contact angle and low water adsorption indicate improved hydrophilicity. Such discrepancy could be partially due to the different durations of the water uptake by the ionomers.

The ionomers' effects on CL wettability also depend on the polarity of the contacting solid components (e.g., carbon materials or catalysts). The hydrophobic backbones tend to interact with the non-polar solid phase, so the polar ionic groups tend to point towards the polar liquid phase and promote wettability.[186] On the other hand, the ionic groups can also re-orient towards the polar surfaces of the solid phase instead of the liquid phase, leaving the hydrophobic backbones exposed to the water phase. In this case, the ionomer in the CL promotes hydrophobicity.[152]

In addition to the chemical properties of the materials, the materials' shape and morphology play a significant role in determining the surface wettability. According to the Wenzel relations, increasing the CL roughness promotes hydrophobicity over the hydrophobic surface and enhances hydrophilicity over hydrophilic surfaces. For example, Hursan et al.[187] reported that introducing pores increases the hydrophobicity of nitrogen-doped carbon CL, where the non-porous material shows an apparent contact angle of 128.5 °. The authors also found that increasing the pore size reduced the bubble residence time and departure diameters. Burdyny et al.[188] reported that the averaged bubble departure diameter decreases in the order of nanoparticles > nanorod > nanoneedles, highlighting that the nanostructured morphology of metals promotes hydrophilicity. One should note that the metal-based catalysts surface commonly undergo restructuring under the CO_2RR conditions [129-132]. The morphology restructuring should also dynamically change the surface properties (e.g., electronic structure and surface chemistry) and consequently affects the wettability and local environment of the catalytic interfaces.[181-184]

3.3 Modification of the gas-diffusion layers

Carbon-based GDLs

As discussed in Section 2.4, GDLs should be hydrophobic to enable gas transport within the structures and prevent aqueous electrolyte entry. The most used GDLs for CO_2RR are carbon-based porous substrates that contain various degrees of hydrophobic materials such as PTFE or silanes.[129, 185] These hydrophobic materials are inserted in both the primary GDL support layer (e.g., carbon fibres and carbon cloth) and the denser microporous layer. A dense MPL is generally needed because the primary support structure contains larger pores (usually in tens of micrometers in diameter), leading to lower capillary pressures. Instead, the microporous layer (MPL) is a non-structural, thin hydrophobic layer with nanosized pores located between the macroporous layer and the CL. The MPL then acts as the primary conductive contact layer with the catalyst layer, the access point for gas diffusion, and the first barrier to electrolyte flooding.

Increasing the loadings of the hydrophobic materials promotes hydrophobicity, but too high loading will decrease the overall electrical conductivity and block the pores for gas diffusions. This trend is well exemplified in Kim et al.'s paper investigating the role of PTFE on Ag-based GDE for CO production.[76] They reported that a 20 wt% PTFE loading in the MPL achieved an optimal CO partial current density (Figure 11a), while a 10 wt% PTFE loading in the macroporous layer (the carbon fiber substrate) showed a higher CO partial current density than the equivalent with 30 or 50 wt% PTFE treatment, which is a result of the slightly higher gas permeability and reduced charge transfer resistance. (Figure 11b and c). Therefore, the microporous layer requires a higher hydrophobicity to maintain a high capillary pressure to resist flooding, while the macroporous layer may not require too

high hydrophobicity at the cost of losing electrical conductivity and pores for gas transport. Table 2 summarizes recent advances in the development of carbon-based GDEs for CO_2RR associated with wettability modification.

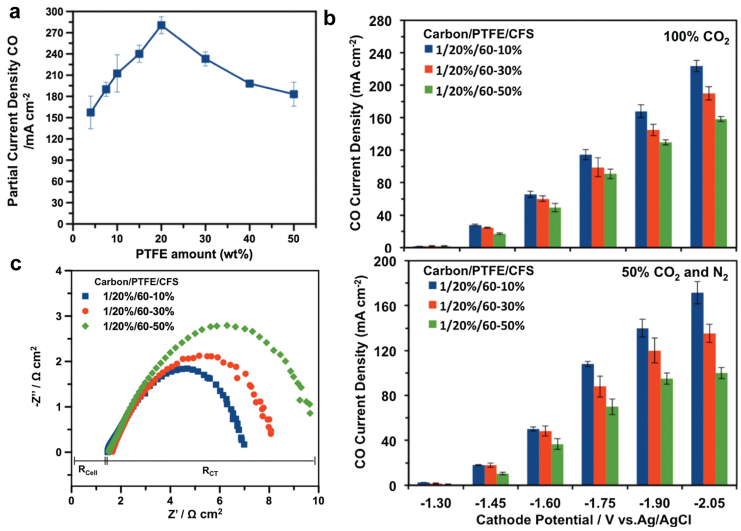

Figure 11 The effects of the PTFE loading of (a) MPL and (b) macroporous layer (denoted as CFS) on the partial current density to produce CO. (c) Effect of the PTFE loading in a macroporous layer on charge-transfer resistance.Reproduced from [76] with permission of Elsevier, copyright 2016.

1

2

3

Table 2 Summary of recent reported carbon-based GDEs for CO_2RR with wettability modified.

Catalyst layer	Additives in CL	GDL	Preparation methods	Potential (V vs RHE)	Faradaic Efficiency (%)								Peak current density (mA cm^{-2})	Catholyte	Membrane	References
					Hydrogen	Formate/formic acid	Carbon monoxide	Methane	Ethelene	Ethanol	Acetate	n-propanol				
SnO_2		Carbon paper (Sigracet 39BC)	Spray the catalyst ink on the carbon paper	-0.80	1.0	83	7						385	0.5 M Na_2CO_3 and 0.5 M Na_2SO_4	Nafion 212	[193]
3D SnO_x nanoparticles/carbon black	Nafion	Carbon GDL	Hydrogen reduced SnO_2 nanoparticles were mixed with carbon black and ionomer in isopropanol and spray coated onto the MPL	-0.98	26.2	64.1	10.3						150	0.5M $KHCO_3$	Nafion 117	[126]
2D SnO_x nanosheets/carbon black			SnO_x nanosheets synthesized via a hydrothermal method, mixed with carbon black and ionomer in isopropanol, and spray coated onto the MPL	-1.03	7.1	77.0	12.4						150	0.5M $KHCO_3$		

Au nanoparticles loaded on carbon black treated with fluorine-terminated silane material	1,1,2,2-perfluorodecyltrimethoxysilane	1wt% PTFE modified carbon fiber papers (TGP-H-60)	Au nanoparticles were loaded on carbon black, treated with the silane, and drop cast onto the PTFE-treated carbon GDL. The silane treatment was conducted by heating the Au/C with the silane coupling agent in stainless steel vessel at 90 °C for 10 min	-0.5			91.7						15.8	1M $KHCO_3$	Nafion 117	137
Au nanoparticles loaded on carbon black			Au nanoparticles were loaded on carbon black and then drop cast onto the PTFE-treated carbon GDL.	-0.5			92.3						89.2	1M $KHCO_3$		
Au nanoparticles loaded on carbon black			Au nanoparticles were loaded on carbon black and then drop-casted onto the PTFE-treated carbon GDL. Finally, treated in an air plasma apparatus for 0.5 min	-0.5			92.1						115.7	1M $KHCO_3$		
Au nanoparticles loaded on carbon black			Au nanoparticles were loaded on carbon black and then drop-casted onto the PTFE-treated carbon GDL. Finally, treated in an air plasma apparatus for 1 min	-0.5			90.6						115.2	1M $KHCO_3$		

Au nanoparticles loaded on carbon black			Au nanoparticles were loaded on carbon black and then drop-casted onto the PTFE-treated carbon GDL. Finally, treated in an air plasma apparatus for 1.5 min	-0.5			89.3						110.1	1M $KHCO_3$		
Au nanoparticles loaded on carbon black			Au nanoparticles were loaded on carbon black and then drop-casted onto the PTFE-treated carbon GDL. Finally, treated in an air plasma apparatus for 2 min	-0.5			88.4						102.5	1M $KHCO_3$		
Au nanoparticles loaded on carbon black			Au nanoparticles were loaded on carbon black, and then drop-casted onto the PTFE-treated carbon GDL. Finally, treated in an air plasma apparatus for 2.5 min	-0.5			86.5						99.7	1M $KHCO_3$		
Ni single-atom	1,1,2,2-perfluorodecyltrimethoxysilane	Carbon fiber from the calcination of polymer fiber via electrospinning	The mixture suspension (PAN, ZIF-8, and $Ni(NO_3)_2 \cdot 6H_2O$dossolved in DMF) was produced into fibers through electrospinning, then carbonized under argon gas, finally were immersed into H_2SO_4 solution to remove the remaining Zn species, Ni or NiO nanoparticles.	-1.0			88.9						405.0	0.5 M $KHCO_3$	Nafion 117	[194]

Ag nanoparticles		Carbon paper (Sigracet 35 BC)	Catalyst ink (Ag nanopowder, deionized water, Nafion binder, and isopropyl alcohol) was airbrushed onto a Sigracet 35 BC GDE carbon paper substrate.	-1.8			95.3						200	3 M KOH	No membrane	54
Ag nanoparticles				-1.7			87.5						200	3 M CSOH		
Ag nanoparticles		Cabon paper (Sigracet 29BC)	Drop-casting the catalyst ink on the carbon paper	-0.6	1.3		97.2						15	1M KOH	Fumasep FAA-3-50	195
Ag nanoparticles		Cabon paper (Freudenberg H23C6)	Spray the catalyst ink on the carbon paper	-2.5 vs Hg/HgO	1.0		97						196	1M KOH	No membrane	53

Cu(OH)F	1,1,2,2-perfluorodecyltrimethoxysilane	Commercial carbon fiber (GDL YLS-30T)	The catalysts were synthesized via hydrothermal treatment of the $Cu(NO_3)_2{\cdot}3H_2O$ and NH_4HF_2 in DMF. Cu(OH)F were dispersed in IPA aqueous solution and then by sonicating for 2 hours to form a homogeneous ink. Finally, the ink was loaded onto the carbon fiber GDL.	-0.6	7.2	4.8	7.8	1.2	57.6	16.9	1.3	5.0	565.1	1M KOH	Anion exchange membrane	[192]
Cu(OH)Cl		Commercial carbon fiber (GDL YLS-30T)	The catalyst was synthesized by using hydrothermal treatment of NH_4Cl and Cu(OH)F in the ethanol-water solution. The subsequent catalyst deposition process was the same as the procedure of Cu(OH)F.	-0.6	11.1	5.4	11.4	0.9	48.9	14.0	2.2	4.8	317.2	1M KOH		
Cu(OH)Br		Commercial carbon fiber (GDL YLS-30T)	The catalyst was synthesized by using hydrothermal treatment of NH_4Br and Cu(OH)F in the ethanol-water solution. The subsequent catalyst deposition process were the same as the procedure of Cu(OH)F.	-0.6	13.0	6.3	16.8	2.2	39.4	13.6	1.6	5.1	265.4	1M KOH		

Cu(OH)I		Commercial carbon fiber (GDL YLS-30T)	The catalyst was synthesized by using hydrothermal treatment of NH_4I and Cu(OH)F in the ethanol-water solution. The subsequent catalyst deposition process were the same as the procedure of Cu(OH)F.	-0.6	16.1	5.1	25.6	2.5	30.4	10.1	1.9	4.1	187.7	1M KOH		
Cu		Commercial carbon fibers (GDL YLS-30T)	The catalyst was synthesized via the hydrothermal treatment of the $Cu(NO_3)_2{\cdot}3H_2O$ in DMF. The collected solid products were washed well before dried in a vacuum. The subsequent procedures were the same as the preparation processes of F–Cu catalyst.	-0.6	17.1	7.3	30.7	2.8	26.9	8.9	1.9	1.3	168.3	1M KOH		
Cu nanoparticles and Cu-MOF (i.e., $Cu_3(BTC)_2$, BTC: 1,3,5-benzene tricarboxylic);		Commercial carbon paper (TGP-H-030)	Cu NPs and Cu-MOF were mixed within IPA at mass ratio (9:1) first and added with Nafion solution. The mixture was coated on the surface of TGP-H-030 and dried.	-2.5 vs SCE	69.2			18.5	7.1					0.5M $NaHCO_3$	Nafion 115	[196]

CuNPs + PTFE	PTFE (30-40 nm)	carbon paper (AvCarb GDS2230)	Commercial Cu nanoparticles, PTFE nanopowder (30–40 nm), and carbon black were dispersed by sonication in IPA, respectively. Afterwards, Cu nanoparticle dispersion, carbon black dispersion, PTFE dispersion, and 200 µL Nafion solution were mixed and sonicated for another 1 h. The above catalyst ink was sprayed on the carbon paper GDL. After drying overnight, diluted PTFE solution was further sprayed on top of all GDEs except the 0% PTFE one.	-1.0	20	11	4	1	31.5	14.5	1		260	1M KOH	Nafion 1110	[145]

Cu oxide nanowires	PTFE particles (50 nm)	oxidized Cu gauze	Wet chemical oxidation method: Cu gauze was firstly immersed in a mixed solution (NaOH and $(NH_4)S_2O_8$). After being rinsed and dried in nitrogen atmosphere, the oxidized Cu gauze was immersed in 10 wt% PTFE dispersion and dried. The coating ink consists of nano-sized carbon black and PTFE particles in the IPA solution. This coating ink was air-brushed onto one side of the oxidized Cu gauze for the formation of a gas diffusion layer. The electrodes were then annealed in a muffle furnace to obtain the final self-supported GDEs.	-0.48	20.2	14.6	24		19.7	4.5		2.3	100.7	1M KOH	anion exchange membrane	[197]

Cu oxide nanowires			Thermal annealing method: cleaned Cu gauze was annealed in a muffle furnace to obtain the Cu oxide nanowires. The coating ink consists of nano-sized carbon black and PTFE particles in the IPA solution. This coating ink was air-brushed onto one side of the oxidized Cu gauze for the formationa of a gas diffusion layer. The electrodes were then annealed in the muffle furnace to obtain the final self-supported GDEs.	-0.49	34.4	9.8	6.5		27.6	6.9		3.1	200.5	1M KOH		

Non-carbon based GDLs

Unfortunately, most of the existing carbon-based GDLs are incapable of preventing electrolyte flooding completely due to electrowetting and the presence of carbons that easily lose their hydrophobicity, particularly in alkaline electrolyte environment.[53, 74, 75] Replacement of the carbon-based GDLs with non-carbon-based GDLs, such as porous hydrophobic polymer substrates[41, 74, 133, 174, 191-194] can significantly improve the capability of the GDL to maintain the hydrophobicity in the harsh CO_2RR conditions either in the catholyte-fed or MEA-based vapor-fed flow cells. Table 3 summarizes recent examples of using non-carbon-based GDLs for CO_2RR.

Table 3 A summary of the recent advances in using non-carbon-based GDLs for CO_2RR.

Catalyst layer	Additives in CL	GDL	Preparation methods	Potential (V vs RHE)	Faradaic Efficiency (%)									Peak current density (mA cm^{-2})	Catholyte	Membrane	References
					Hydrogen	Formate/Formic acid	Carbon monoxide	Methane	Ethylene	Ethanol	Acetate	Ethane	n-Propanol				
3D Cu nanoparticles: ionomer heterojunctions + PFSA coated Cu sputtered on PTFE membrane	Cu(4): PFSA(3)	PTFE GDL	PFSA was first to spray coated on the Cu sputtered on the PTFE membrane, followed by spray coating of Cu nanoparticles and ionomer solution onto the surface.	-0.91	7.9	0.9	6.2		60	13.5	4.5		0.2	1550	7M KOH	Fumasep FAB-PK-130	142
Sputtered Cu with Carbon nanoparticle and graphite layers	Nafion	PTFE GDL	The sputtered Cu PTFE membrane was spray-coated with carbon NP and later with graphite to provide uniform current distribution and overall support	-0.57	6.7	6.2	2.7		69.6	6	5			150	7M KOH	Fumasep FAB-Pk-130	74

Cu nanoparticles mixed with N, N'-ethylene-phenanthrolinium dibromide, and Aquivion ionomer on sputtered Cu	N, N'-ethylene-phenanthrolinium dibromide and Aquivion	PTFE GDL	The sputtered Cu PTFE membrane wasspray-coatedd with Cu nanoparticle, N, N'-ethylene-phenanthrolinium dibromide and Aquivion	-4.205 (cell)	12.9		13.8		66.1					479.6	0.1M KHCO3	Sustainion X37-50	[201]
Titanium dioxide and carbon black with ionomer on sputtered Cu	Sustainion	PTFE GDL	Selected ionomer was mixed together with titanium dioxide and carbon black and spray coated on the Cu sputtered PTFE membrane	-3 (cell)	9	1.5	3.2	1.2	48.2	16	3.6			261.4	1M KOH	N/A	[202]
	Fumion			-3 (cell)	7.3	2.5	2.0	3.8	44.3	17.3	4.4			266.5			
	Nafion			-3 (cell)	2.5	0.2	4.5	0	4.3	1.2	0.1			373.6			
	Aquivion			-3 (cell)	0.6	1.4	4.9	0	1.4	0	0.2			366.6			
Sputtered Ag with carbon nanoparticle	Nafion	PTFE GDL	The sputtered Ag PTFE membrane was spray-coated with carbon nanoparticle mix with Nafion	-0.8	6		88							175	1M KOH	Anion exchange membrane	[198]

20 nm thick Au nanoparticle	N/A	nanoPE membrane	Au is sputtered on the membrane surface and then being fold into an alveolus shape	-0.5	15		85							15	6M KOH in the bilayer and 0.5M		136
Cu Nanoparticle	PFSA	3D printable perfluoropolyether	The GDL is 3D printed and cured The catalyst ink with Cu NP and PFSA is sprayed on the GDL	1.09	21.4	2.1	0.4		36.5	27.6	1.2		2.3	420	1M KHCO3	Fumasep FAB-Pk-130	203
Sputtered Cu with Carbon nanoparticles and graphite layers	Nafion	PTFE GDL	The sputtered Cu PTFE membrane was spray-coated with carbon NP and later with graphite to provide uniform current distribution and overall support	4	5.2	0.3	9.9		46.5	19.4	10.2		1.5	375	0.1M $KHCO_3$	Anion exchange membrane	41
Deposited Cu with Cu(100) facet rich	Nafion	PTFE GDL	catalyst was electrodeposited at -0.4 A cm-2 for 60s on Cu sputtered PTFE GDL in a solution consisting of 0.1 M $CuBr_2$, 0.2 M sodium tartrate dibasic dihydrate and 0.1M KOH	-0.67	7	3	3	0.1	70	10	8		2	284.5	7M KOH	Fumapem FAA-3-PK-130	199

CeO and Cu	Nafion	PTFE GDL	The catalyst was first prepared by dissolving $Ce(NO_3)_3$ and $Cu(NO_3)_2 \cdot 3H_2O$ in DI water, $NH_3.H_2O$ and NaOH for 30 minutes with continuous stirring. Then the suspension was centrifuged and freeze-dried for 24 hours, followed by 600 °C annealing. The solid catalyst formed were then mixed with Nafion, methanol and drop cast of PTFE membrane	-1.12	9.6	7.7	10		47	19.46			8.24	1218	1M KOH	FumasepFAA-3-PK-130	[204]

The most common non-carbon GDL is made from PTFE membranes containing PTFE fibers supported by polypropylene backing layers. These polymeric GDLs are not electronically conductive, so conductive layers such as conformal metal layers (e.g, sputtered Ag or Cu) or carbon materials (e.g., graphite and carbon nanoparticles) need to be added in the GDEs. The coated metal layers usually also perform as the CLs, and the carbon layers could also help stabilize the CLs. With this setup, a high ethylene production can be maintained for 150 hours in 7M KOH aqueous electrolyte at 75-100 mA cm^{-2}, much more stable than the carbon-based counterparts.[74]

The polymer-based GDLs are more flexible with their shape and microstructures than the conventional carbon-based GDL. For example, Li et al.[136] used nanoporous membranes made of polyethylene (PE) to develop a catalytic system mimicking the alveolus structure. After being deposited with Au nanoparticles via magnetron sputtering, the PE membrane was rolled and sealed to form single or bilayer pouch-type structures. The CO_2 gas was supplied internally and electrolyte supplied externally to the CL. As compared to the carbon-based GDL, the nanoporous PE layer shows much higher burst-through pressures and higher stability of the hydrophobicity (water contact angle lowers from 109° to 105° *cf.* 148° to 119°) under CO_2RR conditioning (-1.0 V vs. RHE for 24 h). This means that the nanoPE-based GDL is more resistant to electrolyte flooding and potentially enables fast CO_2 supply to the catalyst site. In addition, with the unique pouch-type designed, the GDL can achieve a much-improved current density and a relatively high local pH (benefiting HER suppression) in the interlayer. By manipulating the spacing of the interlayer, the authors demonstrated the potential to optimize the CO_2RR local environment further to achieve 92% of the FE(CO). This example highlights the high versatility and flexibility of the non-carbon-based GDL to modulate the catalyst local environment via manipulating the polymer's shape, pore size, and structure, which is relatively difficult to achieve over a carbon-based GDLs.

In another recent study, Wicks et al.[203] used the 3D printing technique to optimize the pore structure of the GDL based on a hydrophobic (with a contact angle of 107 – 130 °) perfluoropolyether (PFPE) monolith. (Figure 12a and b) The pores inside the polymers are created by adding pore former (or porogen), which is normally a solvent for the monomer but not for the obtained polymer. The authors used N-methyl pyrrolidone as the solvent and triethylene glycol as the non-solvent for the PFPE monomers at the compositional cloud point to create well-connected pore structures monolith, which was UV-cured, solvent exchanged, and super-critically dried. The CO_2 gas permeance of the GDL can be lowered by increasing the monomer concentrations in the emulsions. (Figure 12c) The CL was prepared by spray coating the Cu nanoparticles with Nafion ionomers. When tested in the presence of 1M $KHCO_3$ aqueous electrolyte, the prepared GDLs with less CO_2 permeance show a lower FE(CO) but a higher FE(C_2H_4). (Figure 12d and e) This trend is consistent with the recent findings that a

moderately high CO_2 local concentration improves the C-C coupling to produce C2 products.[205] Interestingly, the authors found that intensive UV radiation on the monomer emulsions leads to the formation of large pores and uneven gas distributions in the resultant GDLs. (Figure 12f and g) Such uneven distributions cause local regions of low gas diffusivities and a steeper concentration gradient across the GDL, which can increase the residence duration of produced CO near the catalyst surface and promotes further electroreduction to form C2 products.

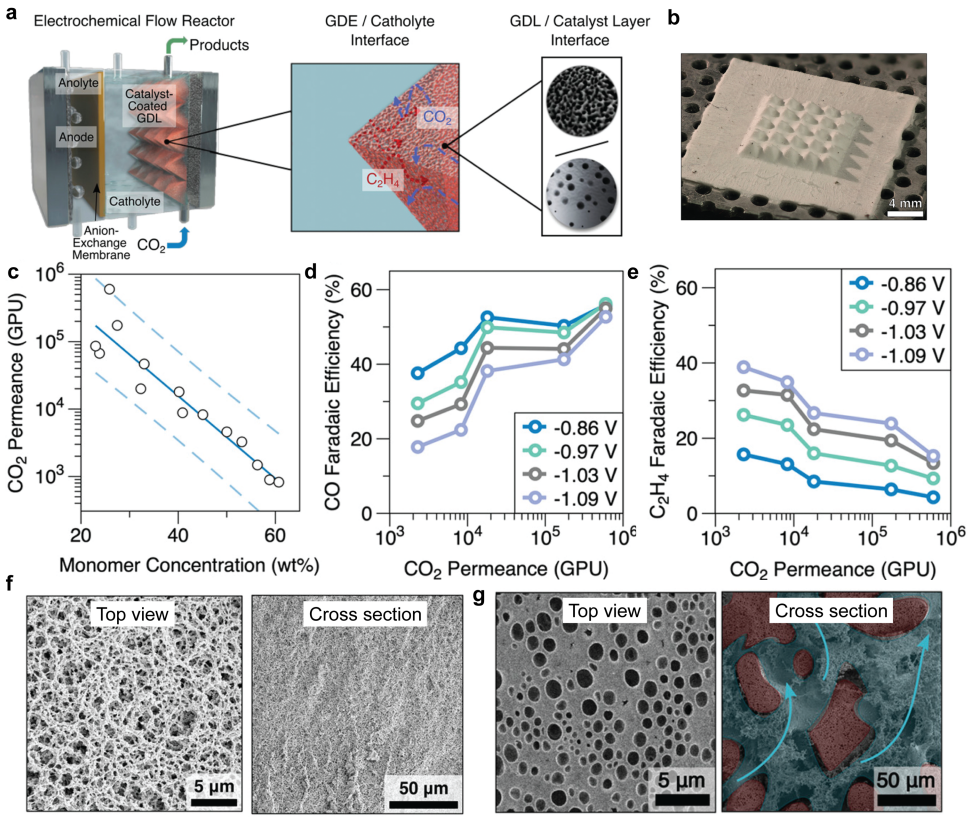

Figure 12 (a) Schematic of the 3D-structured GDL fabricated using 3D printing in a flow cell. (b) A photo of the 3D-printed GDL. (c) The trend of the CO_2 permeance over the GDL prepared from different monomer concentrations of the cloud-point solutions. Effects of the CO_2 permeance on the faradaic efficiencies of (d) CO and (e) C_2H_4. Top-view and cross-sections of (f) the homogeneous PFPE layer cured at about 5 mW cm^{-2} UV intensity and (g) large-pore PFPE layer cured at 200 mW cm^{-2}. Reproduced from [203] with permission of John Wiley and Sons, copyright 2021.

3.4 Tuning the catalyst layer wettability

Reducing catalyst overpotential

As the main driver for electrowetting and electrode flooding, the interfacial electric field can be lowered to improve the electrode wetting stability. This can be achieved by developing a catalyst with reduced onset potentials (the potential at which the reaction starts) and increased density of the active sites. Yang et al.[75] reported that the carbon-based GDLs sputtered with catalyst (i.e., Pt, Cu, and Au) that show more positive potentials for electrochemical reactions (e.g., HER or CO_2RR) are more resistant to the flooding than the ones with more negative potentials to drive the same reaction rate . (Figure 13) Notably, Pt-based GDE shows no flooding when operating at 50 mA cm^{-2} for 3 hours in N_2. Interestingly, they found that Ag- and Cu-based electrodes flood more quickly in N_2 than in CO_2 at 10

mA cm^{-2}, (Figure 13) where these two electrodes showed more positive potentials in CO_2 than in N_2 before the observation of the flooding. These trends suggest that the flooding is likely associated with the activation of the carbon surfaces, which was further confirmed by the loss of F and increased oxygen species at the bare GDL surface. We believe the reported onset potentials partially depend on the PZCs of the catalyst materials, as listed in Table 1. The trend of the measured onset potentials for the metals (Pt < Au< Cu < Ag) in Yang et al.'s work polycrystalline (pc) Ag has a PZC of -0.584 V, much more cathodic than pc-Pt (0.09 - 0.14 V), pc-Cu (0.09 V) and pc-Au (0.2 V). This means one could also manipulate the catalyst material and facets to shift the PZC of catalysts to a more cathodic position, which has not been fully explored in the current literature.

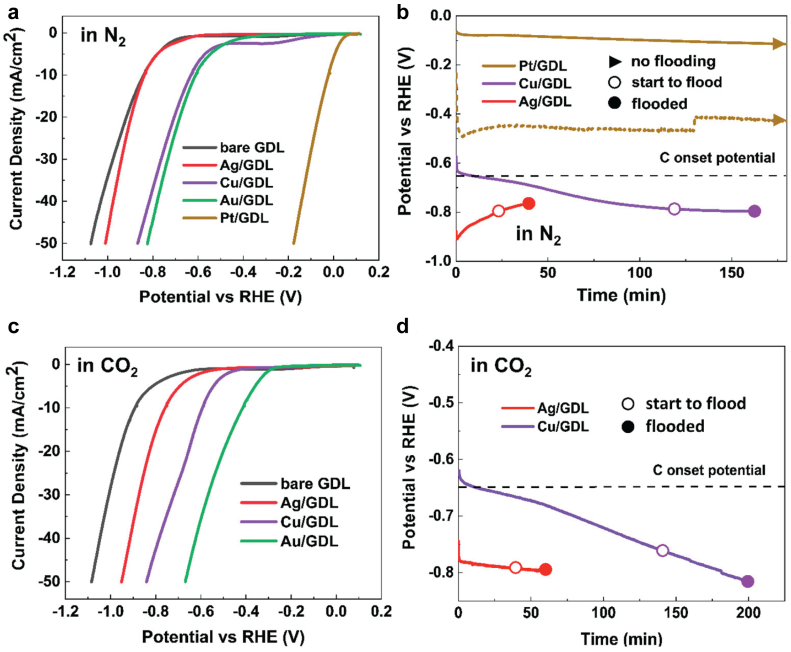

Figure 13 Linear scan voltammograms of the carbon GDL deposited with Ag, Au, Cu, or Pt in 1M $KHCO_3$ in (a) N_2 and (c) CO_2 environment. Potential as a function of time at a constant current of 10 mA cm^{-2} (solid line) and 50 mA cm^{-2} (dashed line) in 1M $KHCO_3$ saturated in (b) N_2 and (d) CO_2 environment. Reproduced from [75] with permission of American Chemical Society, copyright 2021.

<u>Morphological effects on contact angles</u>

There have been tremendous advances in the catalyst development for CO_2RR via optimizing the electronic structures, surface chemistry, microstructures, dimensions, particle sizes, and interparticle distances. This review will not cover detailed strategies to develop catalysts to improve kinetic overpotentials, and we recommend readers to refer to recent catalyst reviews.[3, 5, 199-203] Instead, we will discuss the relations between electrode wettability and catalyst structures.

The catalysts are desired to be liquid wet for CO_2RR catalysis to proceed. If the reaction evolves gases, a hydrophilic (or aerophobic) surface can accelerate the detachment of the gas bubbles, minimizing the loss of the active surface due to the occupancy of the gas bubbles. This strategy has been widely used for other gas-evolving electrolysis, such as hydrogen oxidation reaction and oxygen evolution

reactions for water electrolyzers. [172] The catalysts are usually engineered to nanostructures such as nanosheets or nanoneedles to achieve a highly hydrophilic surface as nanostructured morphology exposes abundant corners or edges, where the atoms show reduced coordination numbers. These under-coordinated atoms interact strongly with adsorbed species or liquid molecules, strengthening the solid-liquid bonds and thus promoting hydrophilicity. For example, Zhao et al.[211] synthesized free-standing carbon paper with vertically aligned single-nickel-atom-based catalysts via the solid-state diffusion method. (Figure 14a) This structure bestows the electrodes with superhydrophilicity with a water contact angle close to 0° and a gas bubble contact angle of 148.3 $\pm$ 2.6 °, which allows a large electrochemical surface area and weakened adsorption of gas bubbles. (Figure 14b) In another study, 1-1.5 wt% PTFE treatment over the carbon nanofibers modified with arrays of Ni-based nitrogen-doped carbon nanotubes (Figure 14c) was found beneficial to enhance FE(CO) and suppress HER (Figure 14d and f) by increasing the water contact angles (Figure 14d) and adhesion forces of gas bubbles with electrode surface (Figure 14e).[212] When the PTFE loading is over 1 wt%, the current densities were lowered due to the loss of the electrochemical surface areas. (Figure 14f) It is important to note that these catalysts were tested over a planar electrode in an H-cell, where CO_2 reaches the catalyst surface via the electrolyte bulk. The reaction at the electrode immersed in the electrolytes may be limited by both the availability of local CO_2 and active sites (wetted catalyst surface), which can be alleviated in a GDE structure. Therefore, the sweet point for GDEs operating at high current densities may shift towards a higher hydrophobicity to ensure sufficient gas transport in the CLs. (See Section 2.4)

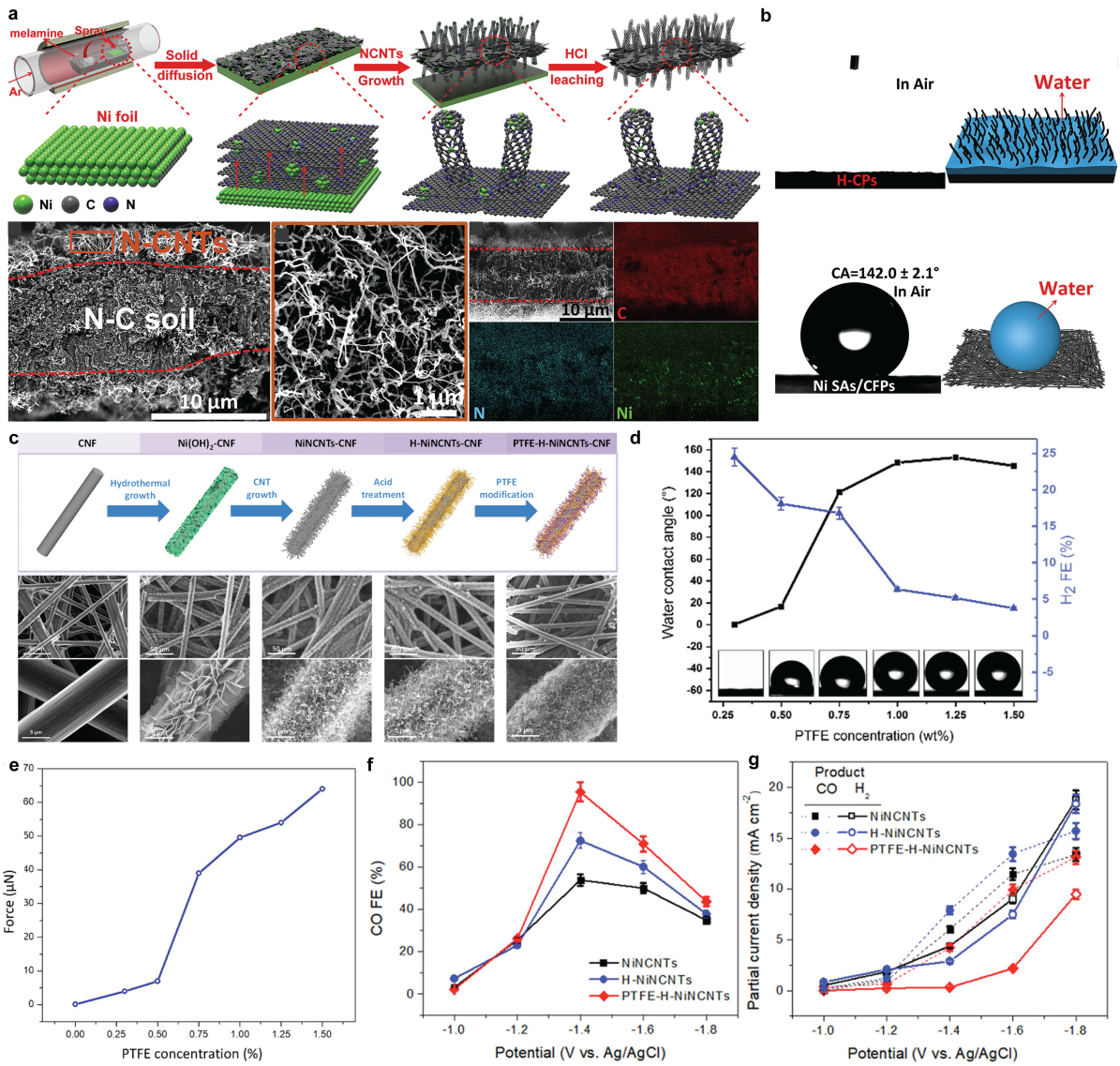

Figure 14 (a) A schematic of the solid-state diffusion method to synthesize carbon papers with vertically-alighted nitrogen-doped carbon nanotubes embedded with nickel single atoms(top) and the SEM images and EDS mapping of the obtained sample. (b) Water contact angles on the obtained carbon paper (top) and nickel single-atoms on carbon fiber-based carbon paper (bottom). Reproduced from [211] with permission of Elsevier, copyright 2019. (c)A schematic of the synthesis method to prepare hierarchical catalysts and the SEM images of the materials at each step. (d) The effects of the PTFE on the apparent water contact angles and the FE(H_2) and adhesive force of the gas bubbles. (f) Faradaic efficiency and (g) partial current densities of CO as a function of potential over NiNCNTs, H-NiNCNTs, and PTFE-H-NiNCNT, as illustrated in (c). Reproduced from [212] with permission of American Chemical Society, copyright 2019.

Addition of hydrophobic materials in the CLs

Hydrophobic particulates such as PTFE nanoparticles can be directly added to the CL to create a hydrophobic microenvironment around the catalysts. The hydrophobic materials need to be pre-mixed with the catalyst materials before catalyst deposition to achieve a uniform dispersion in the CL.[206, 207] The hydrophobic materials are immobilized in the CL through applying either ionomer binders [136, 145] or thermal treatment to soften the hydrophobic materials[151].

In one example, Xing et al.[145] incorporated PTFE nanoparticles with varied loadings and particle sizes in CL by including the PTFE in the catalyst ink (containing Cu nanoparticles, carbon black, and Nafion) for deposition at the GDL surfaces and spraying additional PTFE dispersion solutions at the top CL surface. After CO_2RR conditioning -1.0 V vs. RHE for 1 hour, the 50 wt% of PTFE particles in the CL can successfully sustain the hydrophobicity, with only a small reduction in the water contact angle (Figure 15a). The created hydrophobic microenvironment allows easy gas transport within the CL, leading to much higher CO_2RR current densities and selectivity than the electrode with no PTFE particles. (Figure 15b) However, a too high hydrophobicity (over 60 wt% PTFE) in the CL degraded the CO_2RR current densities (Figure 15c), likely due to the loss of electrochemically-active active sites and the electron conductivities.

This work also demonstrated that the pore sizes could be manipulated by varying the size of the PTFE nanoparticles: small PTFE particles lead to the formation of small hydrophobic pores. According to the Young-Laplace equation (discussed in Section 2.1), small pores are more effective in repelling water than large pores, providing opportunities to resist the liquid intrusion due to electrowetting and maintain the desired wetting condition at CLs. As a result, the CL with smaller size PTFE particles shows higher CO_2RR current densities and faradaic efficiencies and stronger dependencies on the CO_2 feed flow rates. (Figure 15d) The deconvolution of the impedance spectra against equivalent circuit models[215] shows that increasing hydrophobicity significantly reduces the thickness of the diffusion layers from 20.2 ± 3.1 μm for PTFE-free CL to 3.2 ± 0.9 μm for CL included with 50 wt% small PTFE nanoparticles (30-40 nm). The same research group reported a significant improvement of the formate partial current densities up to 677 mA cm^{-2} over Bi-based catalysts with PTFE nanoparticles added. These two studies demonstrate the effectiveness of the addition of PTFE nanoparticles in tuning CL wettability and enhancing local CO_2 mass transport and CO_2RR selectivity.

In another example, the PTFE fine powders were mixed with the SnO_2-loaded carbon black particles by a knife mill for the preparation of the GDE via dry pressing and thermal treatment at 400 °C (above PTFE melting point at 327 °C) for 10 min.[151] In this electrode configuration, PTFE also serves as the binder to keep the electrode structure intact. Consistent with the findings from the last example, a moderate hydrophobicity as achieved by the inclusion of relatively hydrophilic Nafion can lead to an optimal FE(HCOOH) up to 81% with suppressed HER at current densities as high as 1 A cm^{-2}. (Figure 15e) This is likely a consequence of the balanced gas transport and the availability of active sites in the GDE. (Figure 15f) The importance of maintaining the hydrophobic pathways was confirmed by the observed degradation of formate selectivity with the addition of surfactant in the electrolyte, which makes the liquid phase easy to spread and wet the CL pores by reducing the liquid tensions. (Figure 15g)

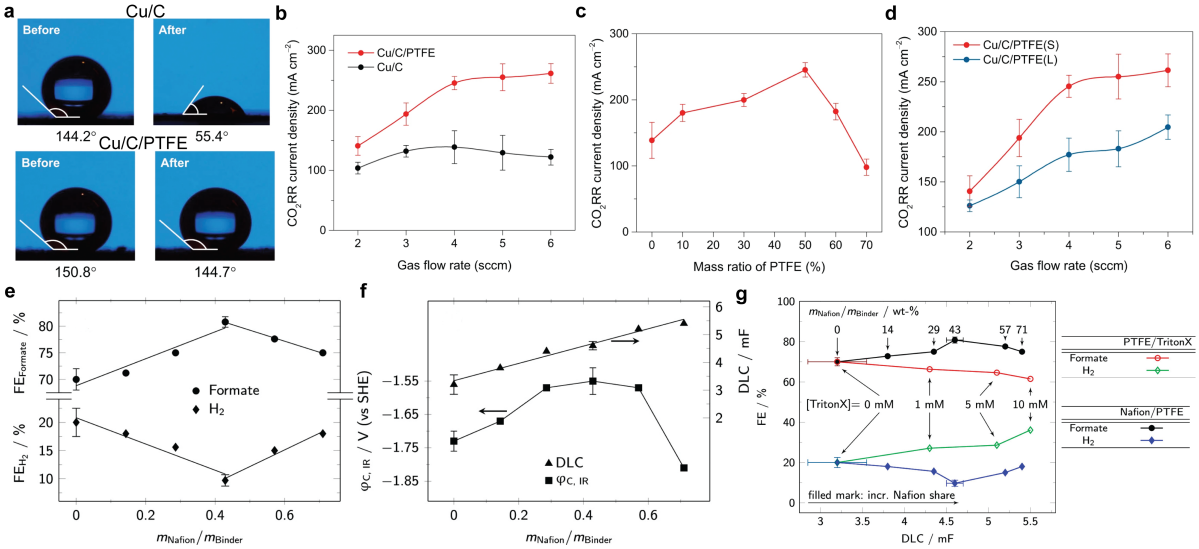

Figure 15 (a) Water contact angles over the CL based on Cu/C and Cu/C/PTFE before and after CO_2RR conditioning at -1.0 V vs. RHE for 2 hours. (b) Dependence of the CO_2RR current densities on the CO_2 feed flow rates over Cu/C and Cu/C/PTFE. (c) Effects of the PTFE loading in the CL on CO_2RR current densities. (d) Comparison of CO_2RR current densities over Cu/C/PTFE CL with different PTFE particle sizes. Reproduced from [145] with permission from Springer Nature, copyright 2021. (e) Faradaic efficiency of H_2 and formate as a function of the binder composition (Nafion and PTFE) of the GDEs based on SnO_2-derived catalysts. (f) iR-compensated cathode potentials and double-layer capacitance as a function of the binder composition. (g) Faradaic efficiency of formate and H_2 over PTFE-bounded GDEs modified with Nafion or surfactant (TritonX) in the electrolyte as a function of the double-layer capacitance. The operating condition for (e-g) is 1 A cm^{-2} in 2M KCl at 50 ℃. Reproduced from [151] with permission of American Chemical Society, copyright 2021.

Addition of ionomers in the CLs

The ionomers such as perfluorinated sulfonic acid (PFSA or commercially available as Nafion) containing hydrophobic backbones can be used to create pathways for gas transport in the CLs.[133, 194] By spray coating the PFSA ionomers or a mixture of Cu nanoparticle and PFSA in a polar solvent onto the Cu-coated PTFE substrate, Arquer et al.[142] developed catalyst-ionomer heterojunctions with significant improvement of the gas diffusion in the CLs without sacrificing electrochemical surface areas. The catalyst structure achieved a notable improvement of the current densities of the gas reduction reactions. Lees et al.[216] reported that the product distribution of Ag-based GDE could vary significantly with the loading of the Nafion ionomers in a zero-gap flow cell. Increasing the loading of ionomers decreases FE(CO) but promotes formate production (peak FE($HCOO^-$) = 31±6% at Nafion loading at 7.5 wt%). In contrast, a too high ionomer loading degrades CO_2RR and promotes HER up to 74±6 % as a result of electrolyte flooding in the cathode and blockage of the pores by the ionomers.

The states of the deposited ionomers, such as molecular conformations, distribution in the CLs, water uptake, and ion conductivity, are strongly influenced by the ionomer chemical parameters (Figure 16a), the ionomer dispersion solvents, and the drying temperatures. How these properties alter the states of deposited ionomers have been widely studied in the field of PEM fuel cells.[210-214] For instance, the dielectric constant and solubility parameters (describing the solvency behavior of the material) of the solvents are key parameters determining the conformation of the PFSA ionomers. Table 4 lists the

detailed solubility parameters and the dielectric constants for the solvents and the PFSAs, as mainly reported by Ma et al..[218] If the solvent (e.g., DMF) has a low solubility parameter close to the PFSA backbone (solubility parameter = 9.7 (cal $cm^{-3})^{1/2}$), there will be fewer hydrophobic backbone aggregates in the solvents, and the hydrophilic sulfonic group tends to be buried inside the PFSA. In the solvents (e.g., methanol-water solvents) with a similar solubility parameter to the PFSA sulfonic group (solubility parameter = 17.3 (cal $cm^{-3})^{1/2}$, the backbone tends to aggregate in the solvents leaving the sulfonate groups in contact with the solvents. A high dielectric constant increases the strengths of the electrostatic repulsion between PFSA molecules, leading to a reduced degree of the backbone aggregations. The large size of the backbone and ionic aggregates normally lead to large pores in the CLs, a high water uptake, and fast proton conduction. Small aggregates are prone to form continuous networks but with small-size pores.[215, 216] Figure 16 shows the schematic illustration of the PFSA structure and the property-wettability relations as summarized by Kusoglu and Weber.[217] In the commonly-used solvents for ionomers for CO_2RR CL preparation, methanol aqueous solution has a higher solubility parameter than ethanol and isopropanol aqueous solutions, resulting in large sizes of hydrophobic and hydrophilic aggregates. These hydrophilic aggregates likely point towards polar catalyst surfaces or carbon materials, leaving the hydrophobic backbones pointing outside to facilitate gas transport.[142] The interactions between ionomer and the solvents may also impact the stability of the ionomers in the CL, particularly when producing liquid products such as alcohols. In contrast, the solvents having a closer solubility parameter to the hydrophobic backbones could help ionomer to form intimate contact with the CL constituents, thus extending the electrochemical surface areas in the CLs.[224] Similarly, the states of the anion-exchange ionomers are also determined by the nature of the solvents.[223]

Table 4 Summary of the solubility parameters and dielectric constants of solvents and Nafion ionomer.[211, 218]

Solvent or ionomer	Solubility parameter (cal $cm^{-3})^{1/2}$	Dielectric constant
Water	23.4	78.4
Methanol	14.5	32.7
Ethanol	12.7	24.5
2-Propanol	11.8	19.9
1-Propanol	11.9	20.1
1-Butanol	11.4	17.8
Ethylene glycol	14.6	31.8
Methanol-water (4/1 g/g)	15.0	32.2
Ethanol-water (4/1 g/g)	14.4	28.5
n-Methylformamide (NMF)	16.1	182.4
(Dimethylformamide) DMF	12.2	36.7

(Dimethylacetamide) DMAc	10.8	37.8
Nafion	9.7 (PFSA backbone), 17.3 (sulfonic group)	-

Increasing the drying temperature accelerates molecular motions and leads to the ordering (or crystalline) of the ionomers. The locally ordered ionomer resists water swelling and thus has a lowered water content (or increased hydrophobicity) and ion conductivity. However, fast evaporation of the solvents resists the movement of the deposited ionomers and thus benefit the formation of a homogeneous distribution of the ionomers in the CLs.[216, 219] Therefore, the solvent properties (e.g., boiling points and viscosity) determining their evaporation processes are also important for the final states of the ionomers in the CLs.

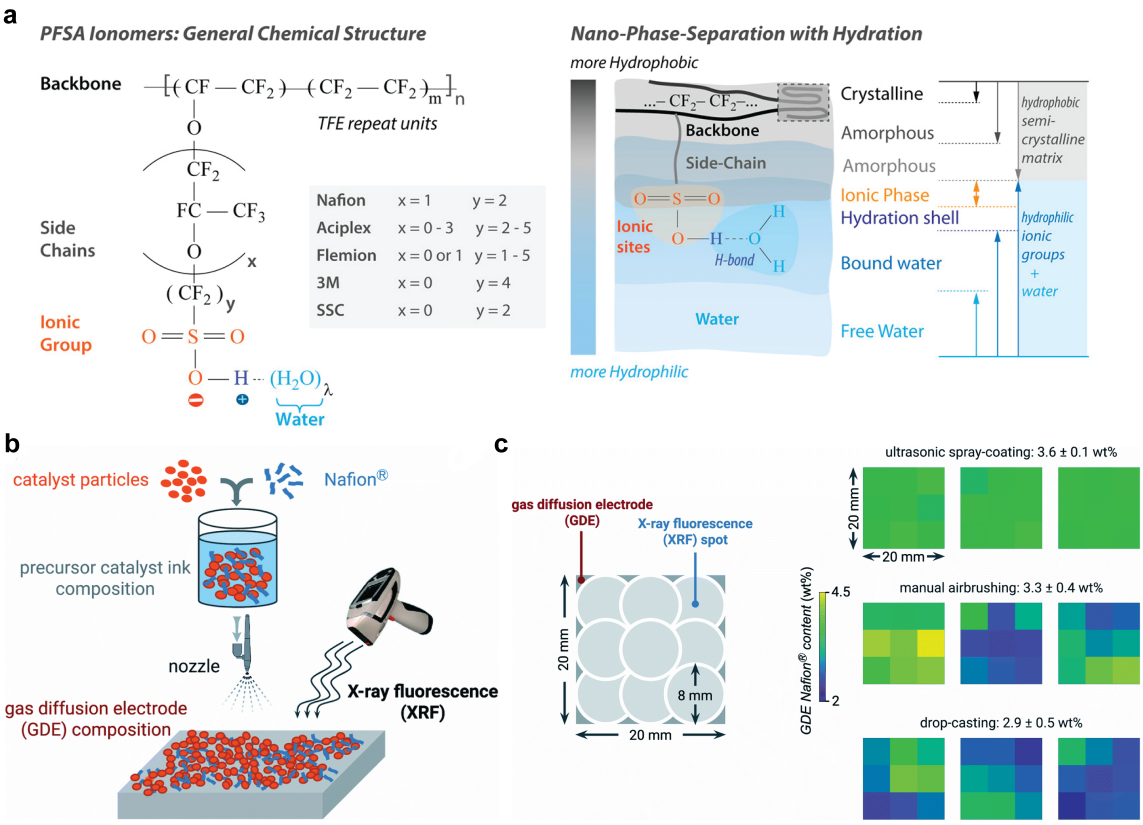

Figure 16 (a) Schematic illustration of the PFSA general structure and the key material factors on ionomers' performance. Reproduced from [217] with permission of American Chemical Society, copyright 2017. (b) Schematic description of the approach to use X-ray fluorescence spectroscopy to investigate the distribution of the ionomers in the CL, and (c) comparison of the ionomer dispersion in the CLs prepared by three different coating techniques. Reproduced from [216] with permission from The Royal Society of Chemistry, copyright 2020.

What also important is the method to fabricate the ionomer-catalyst layers on the GDLs. Lees et al.[216] examined the distribution of the ionomers quantitatively using X-ray fluorescence spectroscopy on the CLs on a 2 x 2 cm^2 prepared by ultrasonic spray coating, manual airbrushing, and drop-casting techniques. (Figure 16b) They reported that the automated ultrasonic spray coating technique generated a more uniform ionomer distribution across the CLs, as evidenced by a much lower spatial

variance of ionomers (0.015 wt%) than the other two techniques (about 0.2 wt%) (Figure 16c). This result is consistent with the qualitative observations by the Kenis group.[227]

Addition of organic modifiers

The catalyst surface can be optimized by surface modification with organic modifiers via coating techniques (e.g., drop or dip coating)[126, 221-223] and electro-dimerization. [193, 224] The organic modifiers are known to influence CO_2RR reactivity and selectivity by changing electrode electronic structures[225-228], altering the binding intermediate binding strength with catalyst surface[175, 229-234] and assisting surface restructuring[242]. Recent studies also showed that the organic modifiers could also alter the wettability of the catalyst surface through changing their nonpolar carbon chain lengths and the types of the polar functional groups and moieties, and thus have an impact on the catalyst surface hydricity and local environment such as pH and availability of water and CO_2. As aforementioned, the primary CO_2RR reaction regimes are located at the liquid-solid interfaces, so hydrophobic treatment of the catalyst surface will lead to loss of the active sites (or reduced electrochemically active surface areas).[53, 126]

Modifying the catalyst surface with hydrophilic or hydrophobic organics can alter the CO_2RR product distribution via modulation of local water availability and metal hydricity (i.e., the energy needed to form a hydride from a metal-H bond).[221, 236] For example, Buckley et al.[228] compared the effects of the organic modifiers on the CO_2RR product selectivity over oxide-derived Cu surface drop coated with these organics. They found that the hydrophilic organics tend to promote formate production and HER, while cationic hydrophobic modifiers enhance CO selectivity. (Figure 17a) This general trend indicates that the bulk properties (in addition to the molecular chemistry[200]) of the organic modifiers also play a role in determining the product distributions likely via influencing catalyst local environment. To elucidate the mechanisms of the modifiers' effects, the authors carried out multiscale ReaxFF reactive molecular dynamics over Cu surfaces modified with two dimethyl substituted ammonium salts with varying lengths of nonpolar hydrocarbon chains. The modeling results unveiled that the modifier with shorter hydrocarbon chains has a water density 1.55 times higher than the one with longer hydrocarbon chains at the Cu surface. (Figure 17b) This is consistent with what we discussed in Section 3.2: the organic modifiers with heteroatoms such as ammonium, phosphonium or oxygen enhance surface hydrophilicity, and the ones with non-polar hydrocarbon chains promote hydrophobicity. More importantly, the authors reported that the hydrophilic surface has a weaker metal-hydride bond than the hydrophobic surface. Therefore, the hydride having weak interaction with the metal surface can be easily added to CO_2 to produce formate. (Figure 17c) In contrast, the CO evolution is not influenced significantly by the strength of the metal-hydride bond,

as the protons needed for CO evolution are sourced from the surrounded water molecules instead of the metal hydride.[244]

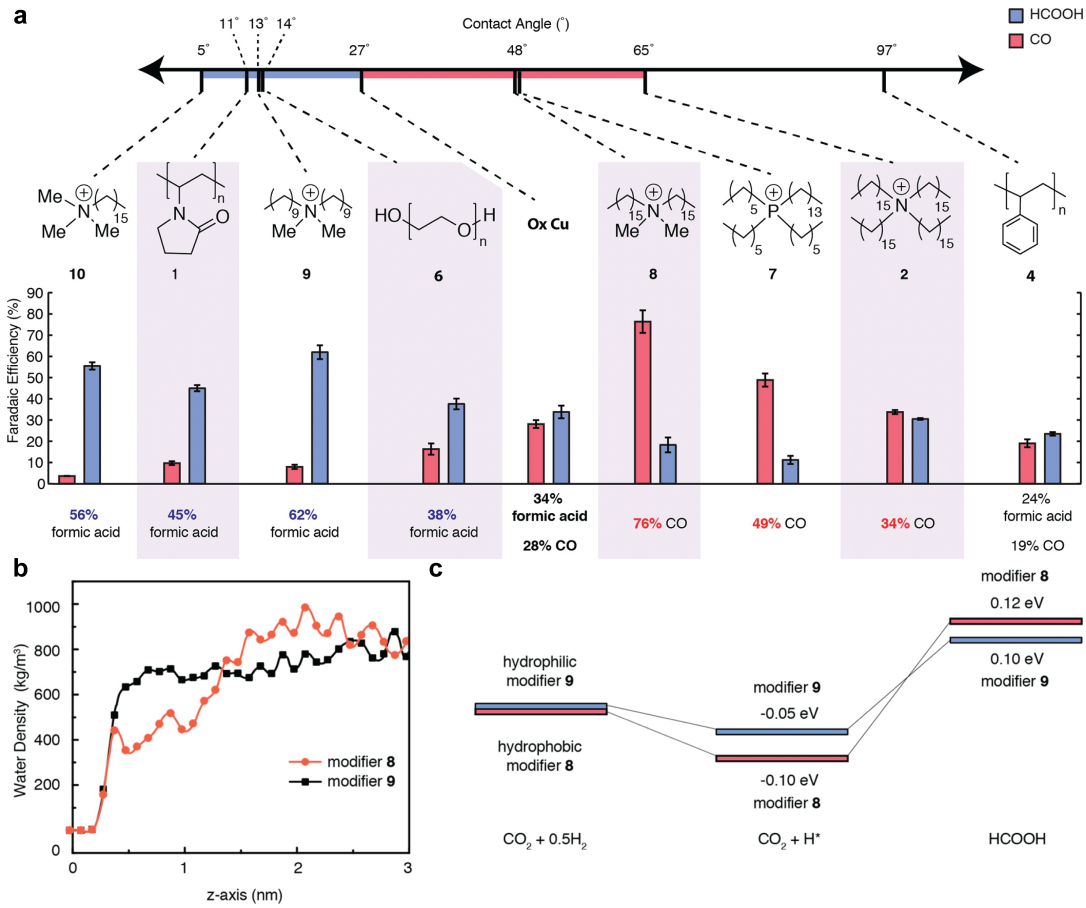

Figure 17 Relations between CO_2RR product selectivity and wettability of the Cu catalyst modified with organic modifiers. (b) Profile of the water density along the z-axis perpendicular to the Cu surface modified with hydrophobic modifier 8 and hydrophilic modifier 9. (c) Predicated energy landscape from ReaxFF to produce formate over modified Cu surface. Reproduced from [228] with permission of American Chemical Society, copyright 2019.

Increasing the hydrophobicity of the catalyst surface prevents catalyst-water contact and can thereby limit the water availability and induce a high concentration of OH^- (i.e., a high local pH) close to the catalyst surface. The restricted water access and increased local pH could both suppress hydrogen evolution, which was widely reported over hydrophobic surfaces, as obtained by either increasing the loading of the hydrophobic materials (e.g., PTFE)[222, 223]or increasing the non-polar hydrocarbon chains.[146, 221] In a very recent study, Liang et al.[154] reported a reduced water diffusion coefficient from 2.35 x 10^{-9} m^2 s^{-1} in the water bulk to 1.81 x 10^{-9} m^2 s^{-1} at close to the surface in the presence of poly(vinylidene fluoride) (PVDF). They demonstrated the dependence of product selectivity on water diffusion coefficient by replacing water with deuterium oxide, which has a relatively low self-diffusion coefficient = 1.87 x 10^{-9} m^2 s^{-1} and hence improves FE(C_2H_4) and reduced FE(H_2) over a Cu catalyst surface. (Figure 18a-c) In addition, the local pH at PVDF-coated surface was calculated to be 9.4, slightly higher than the untreated equivalent (9.2). (Figure 18d) The high local pH, likely resulting from

the limited water diffusion, is the main reason for the promoted C_2H_4 and lowered HER. If containing cations such as quarternary ammoniums, the modifier could also suppress the HER by limiting the proton availability within the electric double layers.[240] Recent results of surface-enhanced infrared adsorption spectroscopy[245] showed a reduced number of water molecules at the presence of cetrimonium bromide (CTAB) in the electrolyte, likely caused by the steric effect and hydrophobic nature of its long carbon chain.

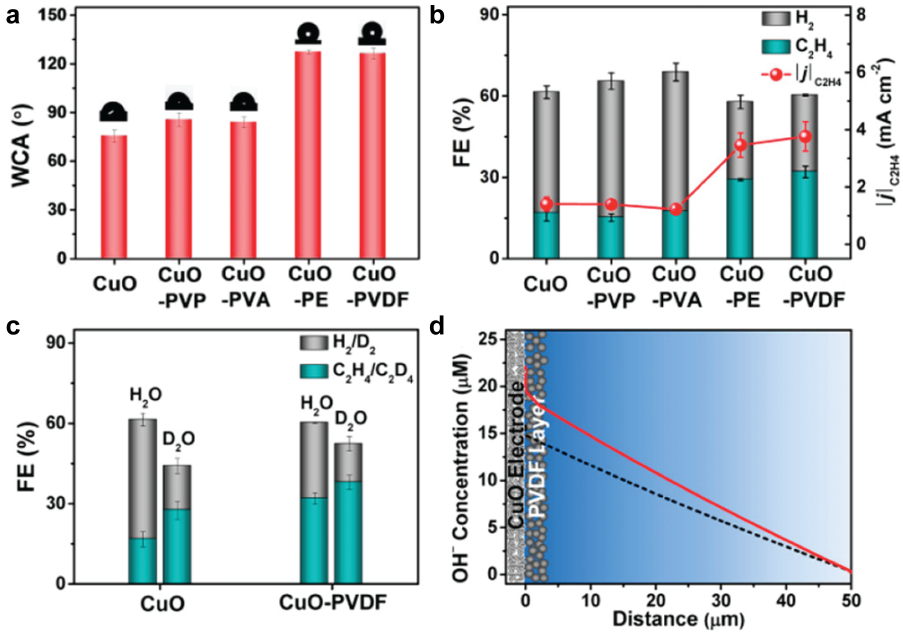

Figure 18 Comparison of the (a) water contact angles (b) product selectivity and partial current densities of CuO and CuO modified with PVP, PVA, PE, and PVDF. (c) Product faradaic efficiency over CuO and CuO-PVDF using water and deuterium oxide as the solvent. (d) Calculated OH^- concentration profile across a 50 μm boundary layer over CuO (black dashed line) and CuO-PVDF (solid red line).Reproduced from [154] with permission of American Chemical Society, copyright 2021.

Product distribution vs. water contact angles

We compared the reported faradaic efficiencies of different products against the water contact angles of the catalysts based on metals such as Cu, Sn, Ag, Au, and Ni in Figure 19. Detailed information can be found in Table S1. The hydrophilic catalyst surfaces tend to produce formate and hydrogen, consistent with the observation by Buckley et al. [228]. For other products such as CO, CH_4, C_2H_4, and alcohols, a moderate wettability (neither too hydrophilic nor hydrophobic) seems beneficial. This trend could be related to the production of CO, which is deemed as one of the reactants for deeper products (e.g., ethylene and alcohols). Evolving CO needs easy desorption of the product, so a slightly hydrophobic catalyst surface should be beneficial for this process. The product distribution is mainly determined by the catalyst materials, applied potentials, and local environment close to the catalysts. The wettability of the catalyst surface plays a role in altering the product selectivity via influencing the catalyst local environment and surface chemistry.

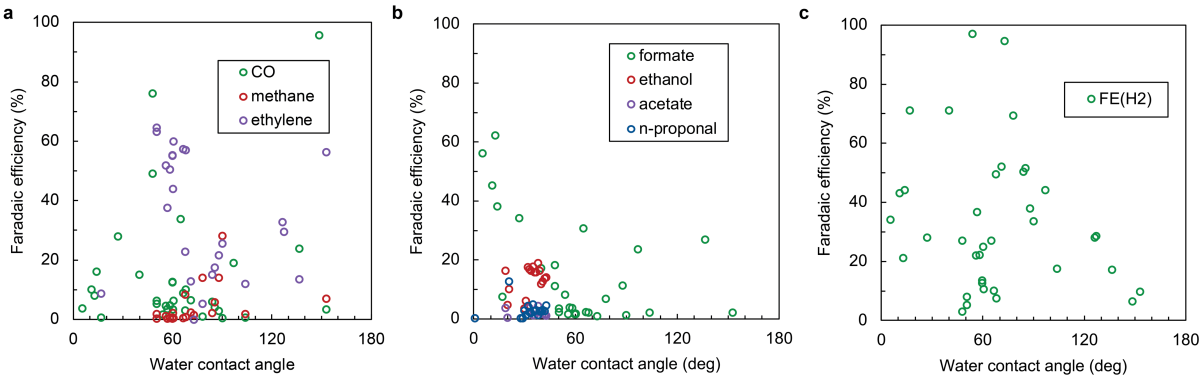

Figure 19 Comparison of the faradaic efficiencies of (a) CO_2RR gas products, (b) CO_2RR liquid products, and (c) H_2 over catalysts with varied wettability.

Stability of the additives

It is also important to maintain a stable modifier-catalyst interface under CO_2RR operating conditions. The modifier–metal surface can interact through chemical bonds such as Cu^+-S [135]or intramolecular forces such as hydrogen bond or electrostatic interactions. These interactions should depend on ligand properties and the catalysts' chemistry and structures. For example, the thiol group (-S-H) can interact strongly with the Cu surface through the Cu^+ - S bond, allowing Wakerley et al. to successfully coat an alkanethiol layer onto the surface of the Cu dendrites and obtain a hydrophobic surface. They reported a small portion of the alkanethiol coating was lost at the catalyst surface close to the electrolyte under CO_2RR conditioning at 15 mA cm^{-2}, likely due to the reduction of Cu^+ to Cu^0. In another study, Wang et al.[246] reported that introducing phenylpyridinium moiety in the polymer-based modifiers can interact strongly with the Cu surface and thus enhance the modifier-Cu surface stability. This leads to much stable faradaic efficiencies of CH_4 and C_2H_4 and good adhesion of the polymer coating after CO_2RR conditioning. (Figure 20) Nafion ionomers are usually used to stabilize the modifier-catalyst surface.[146, 221] It is likely that the nonpolar backbone of the ionomer tends to bind with the hydrophobic modifier, and the polar ionic head groups interact with the hydrophilic metal surface. Zhong et al.[239] found that the surfactants based on branched quarternary ammoniums such as tetraethylammonium ions interact weakly with the Cu surface via electrostatic interactions between negatively charged catalyst surface and positively-charged quaternary ammonium cations, and explained the weak modifier – catalyst interaction arises from the strong tendency for the branched modifier to assemble spherical micelles themselves. In contrast, the ions with one long linear chain, such as cetyltrimethylammonium, tend to form a stable catalyst-modifier bilayer and achieve a more significant improvement of the CO_2RR selectivity. Although the modifier–catalyst interactions remain poorly understood, their interfacial stability is expected to be influenced by the material properties of the catalyst and modifier, local environments (e.g., pH, electrolyte type) and the applied potentials.

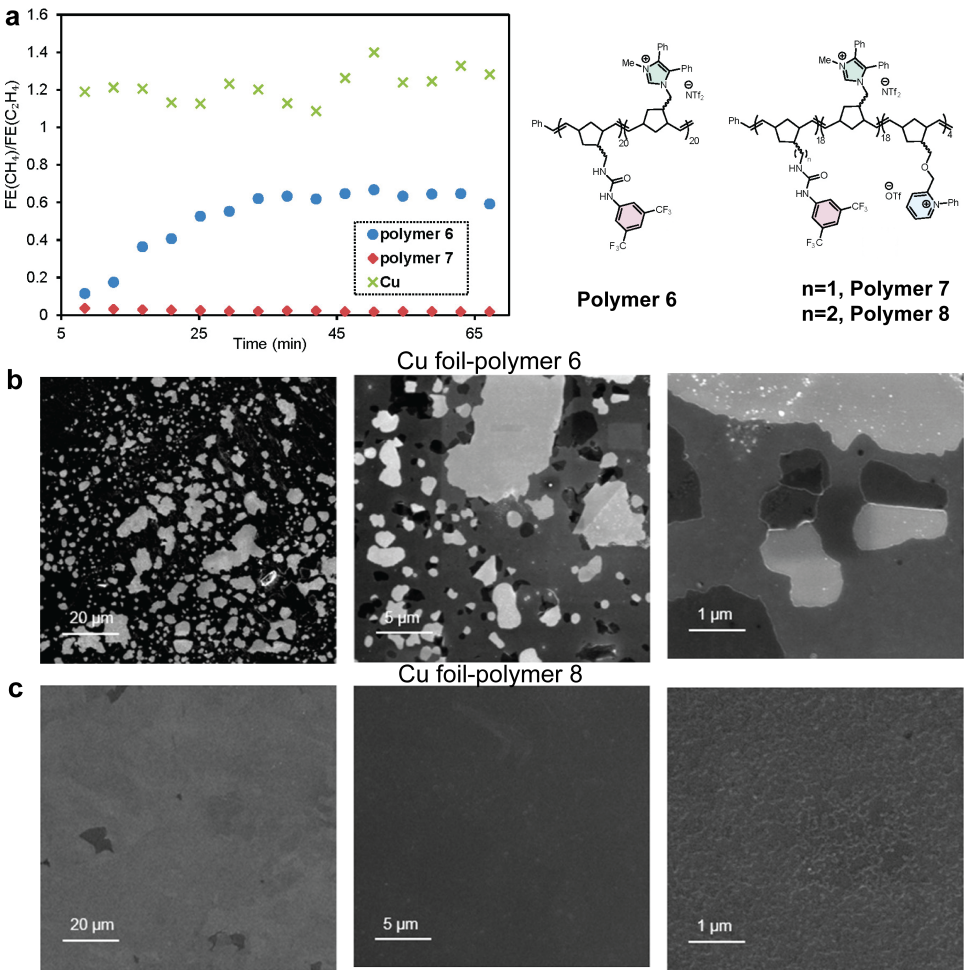

Figure 20 Stability of the faradaic efficiencies of methane over ethylene over Cu foil and Cu foils modified with polymer 6 and 7. Multiscale SEM micrographs of the Cu foil modified with polymer 6 and 8 after CO_2RR conditioning. Reproduced from [246] with permission of American Chemical Society, copyright 2021.

4. Conclusions and outlook

This review described the wetting behavior and desired wetting conditions of the electrode components, including the gas-diffusion layer and catalyst layer under CO_2RR operating conditions, and discusses recent advances in wettability modifications to achieve efficient, selective, and stable CO_2RR performance. The wettability of the electrodes originates from the interfacial interactions between the solid and liquid phases, which strongly depend on the material chemistry, structures and electric field. Properties such as surface chemistry, electronic structures, dimensions, heterogeneity, and microstructures predetermine the wettability and wetting stability of the solid materials, including the catalysts, carbons, hydrophobic polymers, organic additives, and ionomers. How easily the liquid wet the solid surface is also influenced by polarity, ionic nature, and ionic strengths of the liquid electrolytes. The electric field can significantly reduce the electrode wettability by: (1) intensifying the solid-liquid interfacial interactions by re-distributing the charges at the interface; (2) serving a role in the electrochemical capillary pressure that drives the liquid motion in the solid pores; (3) altering the local environment and solid properties that are essential to the electrode wettability.

All these phase properties and operating conditions play significant roles in maintaining an ideal capillary pressure to prevent unwanted electrolyte flooding. These properties are also key contributors to the interfacial electric field, catalytic activity, electron conductivity, and product distribution. Trade-offs usually exist because of the general observations: i.e., (1) strengthened catalyst-liquid interactions benefit CO_2RR but also drive the liquid to wet the pores; (2) hydrophobic pores allow gas transport but diminish electrochemical surface area for CO_2RR. These limitations cause challenges for designing a CO_2RR electrode that is not only active and selective for CO_2RR but also capable of maintaining efficient multiple flows within the electrode.

Recent literature demonstrated exciting opportunities to finely tune the wettability of the electrode via manipulating the material composition, particle sizes, pore structures, surface chemistry, and structures at multiscale, particularly taking advantage of the advances in the fields such as PEM fuel cells, polymer science, and material engineering. Decoupling the gas transport and current distribution functionalities of the gas-diffusion layers, replacing porous carbon matrix (e.g., carbon paper or cloth) with polymer alternatives (e.g., PTFE membranes), has shown its effectiveness to enable stable wetting conditions of the electrode under current densities even higher than 1 A cm^{-2}. The polymer-based GDLs has also demonstrated their potential to precisely control their pore size and structures, which also determine the gas permeance and retention time and provide an alternative avenue to improve the CO_2RR selectivity.

The catalyst layers are where multiple phases interact and the reaction primarily occurs, so wettability needs to be controlled to ensure efficient transport and maximize electrochemical surface area at a macroscale and achieve optimal local environment at catalyst surface in a microscale. Tailoring the hydrophobicity, particle sizes, and morphologies of the additives is effective in adjusting the CL wettability on a macroscale. Designing the chemical structure (e.g., length and branches of carbon chains) and functional groups of the organic molecules is useful to control the wettability of the catalyst surface on a microscale. The micro wettability adjustment may also influence the catalyst surface chemistry and electronic structure, which are also important for CO_2RR catalysis. The stability of the catalyst-modifier interface also relies on the material properties and the conditions of the local environment but remains underexplored by far.

Outlook

Based on the conclusions of this review, we have identified three key scientific questions that need to be addressed to fully understand the wettability degradation modes of the electrodes during CO_2RR and provide new insights to design novel robust and high-performance electrodes.

1. *What are the chemical and physical reasons for the observed permanent loss of hydrophobicity after long-term CO_2RR catalysis at high current densities?* Although recent findings indicate that the permanent loss of electrode hydrophobicity is related to the loss of C-F bonds, deeper investigations are required to understand the mechanisms for the decomposition of fluorinated carbons under CO_2RR operating conditions. Once the electrode pores are flooded, additionally, it becomes very difficult to remove these trapped liquids completely due to the non-cylindrical pores in the fibrous electrode structure. Such residual saturation in the electrode may also lead to the observed loss of the hydrophobicity after high-current CO_2RR operation. Future work could also be meaningful to study the impacts on electrode wetting from the boundary conditions and the steepness of the capillary pressure-saturation relations in the electrode pores, which were demonstrated essential for the diffusion of gas and liquid in the fuel cell electrodes.[247]
2. *What is the role of the potential of zero charge in determining the electrowetting behavior in both GDLs and CLs?* As discussed in Section 2.2, the PZCs values are important properties affecting the actual interfacial electric field, which determines the conditions of the electric double layer and the degree of the electric potential impact on wettability change. Therefore, both theoretical and experimental studies on the PZCs and their roles in the CO_2RR could shed light on answering this question.
3. *How does the catalytic interfaces with varied wettability affect the local intensity of the electric field?* Increasing hydrophobicity in the CLs causes loss of the electrochemically active surface area, which should intensify the local electric field to drive the same current densities. This is expected to profoundly impact large-area electrodes where homogeneity is highly desired but challenging to achieve.

Based on the discussion of the electrode wettability in Sections 2 and 3, we believe the following future directions are worthy of being explored when pursuing the desired wetting conditions for the next generation of GDEs at commercially relevant current densities.

Re-design the microstructure and chemistry of the microporous layer

The existing microporous layer, particularly for carbon-based electrodes, is a thin layer packed with carbon materials and hydrophobic materials (PTFE) with nanovoids to allow gas transport. This design seems challenging to handle the wetting conditions during CO_2RR catalysis. Tailoring the pore structures and thicknesses of the microporous layer remain underexplored but should have profound impacts on the product distributions and transport phenomena, which has been proved by recent research work by Wicks et al.[203], who manipulated the pore structures of the polymer-based GDL via 3D printing techniques. Porous carbon matrix with controllable pore structures can be achieved via

carbonization, chemical activation, templating, and self-templating methods.[242-244] These advanced preparation methods could provide new opportunities to precisely control the pore structures of the MPLs.

Besides, the PZC values of the electrically conducting carbon materials in the MPL can be shifted towards a more negative value through surface modification, such as the incorporation of polymers with positively charged functional groups. A more negative PZC weakens the actual interfacial electric field and thus resists electrowetting.

A patterned electrode surface could be another strategy to weaken the local interfacial field and therefore reduce the degree of electrowetting by increasing the density of active sites. This strategy has been widely used in PEM fuel cell developments[245, 246], and could be valid in the case of CO_2RR as long as the transport of the multiphase flows are carefully managed.[203]

Re-design the catalyst layer

Similar to the GDL design, decoupling the functions of the CL components has the potential to resolve the challenges to balancing the transport and reactions. The materials used to construct the gas, liquid, and electron pathways in the CLs should be separated so that the hydrophobic materials benefiting gas transport may not be concerned about reduced electrochemical surface area and low CO_2RR activity, while hydrophilic catalysts active for CO_2RR may not face challenges to maintain gas pathways. Again, the electron conductor such as carbon can be further modified to resist flooding while sustaining a low ohmic loss to distribute the current. This concept was proved effective to optimize the wetting conditions by recent research attempts such as the addition of PTFE nanoparticles in the CLs[136, 143] or plasma treatment to introduce oxygen-containing groups in catalyst support based on carbon black[137].

Additionally, if we reconsider the electrolyte flooding as a position shift of the gas-liquid interfaces from the liquid side to the gas side, the CL may not be necessarily only at the interface in between the GDL and electrolyte or membrane. Alternatively, the catalyst can be embedded in the GDLs with a loading profile across the electrode. Therefore, the CO_2 starvation issue due to flooding might be alleviated.

Reactor configuration reconsideration

The emerging membrane electrode assemblies[14, 247-250] for CO_2RR show promise to limit the availability of liquid in the GDEs, though salts precipitation and dehydration become critical issues for long-term stability.[23, 247, 251, 252] This review has a main focus on the flow-by mode, but the flow-through mode worth further exploration. In flow-through mode, a high gas to liquid pressure drop can be maintained

via pumping so that wettability control in the catalyst layer could be simplified to just maintain maximized liquid-wet surface. The recent work by Rabiee et al.[46] highlighted the important role of hydrophilic BiOx catalyst surface on the GDE based on Cu hollow fibers in boosting the performance to produce formate.

Acknowledgment

We acknowledge funding towards our research activities related to this review received from the UQ Foundation Research Excellence Award, and the Australian Research Council (LP160101729, FL170100101). Y. Wu and M. N. Idros acknowledge scholarship support from the University of Queensland (UQ) Graduate School. T.Burdyny acknowledges NWO for an individual Veni grant.

Declaration of interest

There are no conflicts to declare.

List of acronyms

Acronym	Definition
AEM	Anion-exchange membrane
C2	CO_2 electrochemical reduction products containing two carbon atoms
CL	Catalyst layer
CLSM	Confocal laser scanning microscopy
CO_2	Carbon dioxide
CO_2RR	CO_2 electrochemical reduction
ECP	Electrical capillary pressure
EDL	Electric double-layer
FE	Faraday efficiency
GDE	Gas-diffusion electrode
GDL	Gas diffusion layer
HER	Hydrogen evolution reaction
MPL	Microporous layer
PE	Polyethylene
PEM	Proton-exchange membrane
PFSA	Perfluorinated sulfonic acid
PTFE	Polytetrafluoroethylene
PZC	Potential of zero charge

5. References

1. IRENA, *Renewable Power Generation Costs in 2019*, 2019.
2. R. I. Masel, Z. Liu, H. Yang, J. J. Kaczur, D. Carrillo, S. Ren, D. Salvatore and C. P. Berlinguette, *Nat. Nanotechnol.*, 2021, **16**, 118-128.
3. M. Li, S. Garg, X. Chang, L. Ge, L. Li, M. Konarova, T. E. Rufford, V. Rudolph and G. Wang, *Small Methods*, 2020, **4**, 2000033.

4. S. Nitopi, E. Bertheussen, S. B. Scott, X. Liu, A. K. Engstfeld, S. Horch, B. Seger, I. E. L. Stephens, K. Chan, C. Hahn, J. K. Nørskov, T. F. Jaramillo and I. Chorkendorff, *Chem. Rev.*, 2019, **119**, 7610-7672.
5. A. Wagner, C. D. Sahm and E. Reisner, *Nat. Catal.*, 2020, **3**, 775-786.
6. D.-H. Nam, P. De Luna, A. Rosas-Hernández, A. Thevenon, F. Li, T. Agapie, J. C. Peters, O. Shekhah, M. Eddaoudi and E. H. Sargent, *Nat. Mater.*, 2020, **19**, 266-276.
7. S. Ren, D. Joulié, D. Salvatore, K. Torbensen, M. Wang, M. Robert and C. P. Berlinguette, *Science*, 2019, **365**, 367-369.
8. Y. Cheng, S. Yang, S. P. Jiang and S. Wang, *Small Methods*, 2019, **3**, 1800440.
9. T. N. Nguyen and C.-T. Dinh, *Chem. Soc. Rev.*, 2020, **49**, 7488-7504.
10. D. Higgins, C. Hahn, C. Xiang, T. F. Jaramillo and A. Z. Weber, *ACS Energy Lett.*, 2019, **4**, 317.
11. H. Rabiee, L. Ge, X. Zhang, S. Hu, M. Li and Z. Yuan, *Energy Environ. Sci.*, 2021, **14**, 1959-2008.
12. R. B. Kutz, Q. Chen, H. Yang, S. D. Sajjad, Z. Liu and I. R. Masel, *Energy Technol.*, 2017, **5**, 929-936.
13. D. A. Salvatore, C. M. Gabardo, A. Reyes, C. P. O'Brien, S. Holdcroft, P. Pintauro, B. Bahar, M. Hickner, C. Bae, D. Sinton, E. H. Sargent and C. P. Berlinguette, *Nat. Energy*, 2021, **6**, 339-348.
14. Z. Yan, J. L. Hitt, Z. Zeng, M. A. Hickner and T. E. Mallouk, *Nature Chem.*, 2021, **13**, 33-40.
15. B. Endrődi, E. Kecsenovity, A. Samu, T. Halmágyi, S. Rojas-Carbonell, L. Wang, Y. Yan and C. Janáky, *Energy Environ. Sci.*, 2020, **13**, 4098-4105.
16. L. Fan, C. Xia, F. Yang, J. Wang, H. Wang and Y. Lu, *Science Advances*, 2020, **6**, eaay3111.
17. D. M. Weekes, D. A. Salvatore, A. Reyes, A. Huang and C. P. Berlinguette, *Acc. Chem. Res.*, 2018, **51**, 910-918.
18. B. Skinn, *Microfluidic System for CO₂ Reduction to Hydrocarbons (Phase II Final Report)*, United States, 2020.
19. W. A. Smith, T. Burdyny, D. A. Vermaas and H. Geerlings, *Joule*, 2019, **3**, 1822-1834.
20. S. van Bavel, S. Verma, E. Negro and M. Bracht, *ACS Energy Lett.*, 2020, **5**, 2597-2601.
21. T. Haas, R. Krause, R. Weber, M. Demler and G. Schmid, *Nat. Catal.*, 2018, **1**, 32-39.
22. J. A. Rabinowitz and M. W. Kanan, *Nat. Commun.*, 2020, **11**, 5231.
23. L.-C. Weng, A. T. Bell and A. Z. Weber, *Energy Environ. Sci.*, 2019, **12**, 1950-1968.
24. N. S. Romero Cuellar, C. Scherer, B. Kaçkar, W. Eisenreich, C. Huber, K. Wiesner-Fleischer, M. Fleischer and O. Hinrichsen, *J. CO2 Util.*, 2020, **36**, 263-275.
25. M. Jouny, G. S. Hutchings and F. Jiao, *Nat. Catal.*, 2019, **2**, 1062-1070.
26. A. Ozden, Y. Wang, F. Li, M. Luo, J. Sisler, A. Thevenon, A. Rosas-Hernández, T. Burdyny, Y. Lum, H. Yadegari, T. Agapie, J. C. Peters, E. H. Sargent and D. Sinton, *Joule*, 2021, **5**, 706-719.
27. M. H. Barecka, J. W. Ager and A. A. Lapkin, *Energy Environ. Sci.*, 2021, **14**, 1530-1543.
28. CERT, https://carbon.xprize.org/prizes/carbon/teams/cert, (accessed 1 April 2021).
29. J. J. Kaczur, H. Yang, Z. Liu, S. D. Sajjad and R. I. Masel, *Front. chem.*, 2018, **6**.
30. S. a. Evonik, CO2 for a clean performance: Rheticus research project enters phase 2, https://press.siemens.com/global/en/pressrelease/research-project-rheticus, (accessed 1 April, 2021).
31. R. Krause, D. Reinisch, C. Reller, H. Eckert, D. Hartmann, D. Taroata, K. Wiesner-Fleischer, A. Bulan, A. Lueken and G. Schmid, *Chem. Ing. Tech.*, 2020, **92**, 53-61.
32. R. K. B. Karlsson and A. Cornell, *Chem. Rev.*, 2016, **116**, 2982-3028.
33. W. R. Leow, Y. Lum, A. Ozden, Y. Wang, D.-H. Nam, B. Chen, J. Wicks, T.-T. Zhuang, F. Li, D. Sinton and E. H. Sargent, *Science*, 2020, **368**, 1228-1233.
34. L. Yang, W. Liu, Z. Zhang, X. Du, L. Dong and Y. Deng, *J. Power Sources*, 2019, **420**, 99-107.
35. S. Verma, S. Lu and P. J. A. Kenis, *Nat. Energy*, 2019, **4**, 466-474.
36. Q. Wang, W. Wang, C. Zhu, C. Wu and H. Yu, *J. CO2 Util.*, 2021, **47**, 101497.
37. J. Na, B. Seo, J. Kim, C. W. Lee, H. Lee, Y. J. Hwang, B. K. Min, D. K. Lee, H.-S. Oh and U. Lee, *Nat. Commun.*, 2019, **10**, 5193.

38. Y. Hori, in *Modern Aspects of Electrochemistry*, eds. C. G. Vayenas, R. E. White and M. E. Gamboa-Aldeco, Springer New York, New York, NY, 2008, vol. 42, pp. 89-189.
39. C. Xia, P. Zhu, Q. Jiang, Y. Pan, W. Liang, E. Stavitski, H. N. Alshareef and H. Wang, *Nat. Energy*, 2019, **4**, 776-785.
40. J. Lee, J. Lim, C.-W. Roh, H. S. Whang and H. Lee, *J. CO2 Util.*, 2019, **31**, 244-250.
41. C. M. Gabardo, C. P. O'Brien, J. P. Edwards, C. McCallum, Y. Xu, C.-T. Dinh, J. Li, E. H. Sargent and D. Sinton, *Joule*, 2019, **3**, 2777-2791.
42. L.-C. Weng, A. T. Bell and A. Z. Weber, *Phys. Chem. Chem. Phys.*, 2018, **20**, 16973-16984.
43. N. T. Nesbitt, T. Burdyny, H. Simonson, D. Salvatore, D. Bohra, R. Kas and W. A. Smith, *ACS Catal.*, 2020, **10**, 14093-14106.
44. T. Burdyny and W. A. Smith, *Energy Environ. Sci.*, 2019, **12**, 1442-1453.
45. R. Kas, K. K. Hummadi, R. Kortlever, P. de Wit, A. Milbrat, M. W. J. Luiten-Olieman, N. E. Benes, M. T. M. Koper and G. Mul, *Nat. Commun.*, 2016, **7**, 10748.
46. H. Rabiee, L. Ge, X. Zhang, S. Hu, M. Li, S. Smart, Z. Zhu and Z. Yuan, *Appl. Catal., B*, 2021, **286**, 119945.
47. H. Rabiee, X. Zhang, L. Ge, S. Hu, M. Li, S. Smart, Z. Zhu and Z. Yuan, *ACS Appl. Mater. Interfaces*, 2020, **12**, 21670-21681.
48. M. König, J. Vaes, E. Klemm and D. Pant, *iScience*, 2019, **19**, 135-160.
49. S. Garg, M. Li, A. Z. Weber, L. Ge, L. Li, V. Rudolph, G. Wang and T. E. Rufford, *J. Mater. Chem. A*, 2020, **8**, 1511-1544.
50. S. Ringe, E. L. Clark, J. Resasco, A. Walton, B. Seger, A. T. Bell and K. Chan, *Energy Environ. Sci.*, 2019, **12**, 3001-3014.
51. D. R. Lide, *CRC Handbook of Chemistry and Physics, 85th Edition*, Taylor & Francis, 2004.
52. S. Veran-Tissoires, M. Marcoux and M. Prat, *Phys. Rev. Lett.*, 2012, **108**, 054502.
53. M. E. Leonard, L. E. Clarke, A. Forner-Cuenca, S. M. Brown and F. R. Brushett, *ChemSusChem*, 2020, **13**, 400-411.
54. E. R. Cofell, U. O. Nwabara, S. S. Bhargava, D. E. Henckel and P. J. A. Kenis, *ACS Applied Materials & Interfaces*, 2021, **13**, 15132-15142.
55. M. B. Ross, P. De Luna, Y. Li, C.-T. Dinh, D. Kim, P. Yang and E. H. Sargent, *Nat. Catal.*, 2019, **2**, 648-658.
56. M.-Y. Lee, K. T. Park, W. Lee, H. Lim, Y. Kwon and S. Kang, *Crit. Rev. Environ. Sci. Technol.*, 2020, **50**, 769-815.
57. L. Sun, V. Reddu, A. C. Fisher and X. Wang, *Energy Environ. Sci.*, 2020, **13**, 374-403.
58. J. Resasco and A. T. Bell, *Trends Chem.*, 2020, **2**, 825-836.
59. W. Ren and C. Zhao, *Natl. Sci. Rev.*, 2019, **7**, 7-9.
60. J. Lee, W. Lee, K. H. Ryu, J. Park, H. Lee, J. H. Lee and K. T. Park, *Green Chem.*, 2021, **23**, 2397-2410.
61. L. Yeo, in *Encyclopedia of Microfluidics and Nanofluidics*, ed. D. Li, Springer US, Boston, MA, 2008, DOI: 10.1007/978-0-387-48998-8_1696, pp. 2186-2196.
62. E. Hadjittofis, S. C. Das, G. G. Z. Zhang and J. Y. Y. Heng, in *Developing Solid Oral Dosage Forms (Second Edition)*, eds. Y. Qiu, Y. Chen, G. G. Z. Zhang, L. Yu and R. V. Mantri, Academic Press, Boston, 2017, pp. 225-252.
63. T. Young, *Philos. Trans. R. Soc. London*, 1805, **95**, 65-87.
64. D. Bonn, J. Eggers, J. Indekeu, J. Meunier and E. Rolley, *Rev. Mod. Phys.*, 2009, **81**, 739-805.
65. R. N. Wenzel, *Industrial & Engineering Chemistry*, 1936, **28**, 988-994.
66. D. Quéré, *Annu. Rev. Mater. Res.*, 2008, **38**, 71-99.
67. E. D. Laird, R. K. Bose, H. Qi, K. K. S. Lau and C. Y. Li, *ACS Appl. Mater. Interfaces*, 2013, **5**, 12089-12098.
68. E. Bormashenko, R. Pogreb, S. Balter and D. Aurbach, *Sci. Rep.*, 2013, **3**, 3028.
69. E. W. Washburn, *Phys. Rev.*, 1921, **17**, 273-283.

70. D. Bohra, J. H. Chaudhry, T. Burdyny, E. A. Pidko and W. A. Smith, *Energy Environ. Sci.*, 2019, **12**, 3380-3389.
71. G. I. Guerrero-García, E. González-Tovar, M. Chávez-Páez, J. Kłos and S. Lamperski, *Phys. Chem. Chem. Phys.*, 2018, **20**, 262-275.
72. L. Yeo and H.-C. Chang, in *Encyclopedia of Microfluidics and Nanofluidics*, ed. D. Li, Springer US, Boston, MA, 2008, DOI: 10.1007/978-0-387-48998-8_470, pp. 600-606.
73. F. Mugele and J. Heikenfeld, in *Electrowetting*, 2018, DOI: https://doi.org/10.1002/9783527412396.ch4, pp. 113-131.
74. C.-T. Dinh, T. Burdyny, M. G. Kibria, A. Seifitokaldani, C. M. Gabardo, F. P. García de Arquer, A. Kiani, J. P. Edwards, P. De Luna, O. S. Bushuyev, C. Zou, R. Quintero-Bermudez, Y. Pang, D. Sinton and E. H. Sargent, *Science*, 2018, **360**, 783-787.
75. K. Yang, R. Kas, W. A. Smith and T. Burdyny, *ACS Energy Lett.*, 2021, **6**, 33-40.
76. B. Kim, F. Hillman, M. Ariyoshi, S. Fujikawa and P. J. A. Kenis, *J. Power Sources*, 2016, **312**, 192-198.
77. J. Huang, P. Li and S. Chen, *Physical Review B*, 2020, **101**, 125422.
78. T. Wu, G. Wang, F. Zhan, Q. Dong, Q. Ren, J. Wang and J. Qiu, *Water Res.*, 2016, **93**, 30-37.
79. D. Ma, Y. Wang, X. Han, S. Xu and J. Wang, *Sep. Purif. Technol.*, 2017, **189**, 467-474.
80. S. Ringe, C. G. Morales-Guio, L. D. Chen, M. Fields, T. F. Jaramillo, C. Hahn and K. Chan, *Nat. Commun.*, 2020, **11**, 33.
81. L. Khmelevaya, A. Chizhov, B. Damaskin and T. Vainblat, *Elektrokhimiya*, 1980, **16**, 257-260.
82. V. SAFONOV, B. DAMASKIN and M. CHOBA, *Èlektrohimiâ*, 1989, **25**, 1432-1438.
83. V. MISHUK, E. SOLOMATIN and V. ELKIN, *SOVIET ELECTROCHEMISTRY*, 1978, **14**, 986-987.
84. J. Carr, N. Hampson, S. Holley and R. Taylor, *J. Electroanal. Chem. Interfacial Electrochem.*, 1971, **32**, 345-352.
85. V. Y. Bartenev, E. Sevastyanov and D. Leikis, *Elektrokhimiya*, 1970, **6**, 1868-1870.
86. U. Palm and V. Past, *Russ. Chem. Rev.*, 1975, **44**, 965.
87. L. KHMELEVAYA and B. DAMASKIN, *Journal*, 1981, **17**, 1441-1444.
88. E. Lust, A.-Y. Yanes, K. Lust and Y. I. Erlikh, *Russ. J. Electrochem.*, 1996, **32**, 552-564.
89. E. Lust, K. Lust and A.-J. Jänes, *Russ. J. Electrochem.*, 1995, **31**, 807-821.
90. G. Valette and A. Hamelin, *J. Electroanal. Chem.*, 1973, **45**, 301-319.
91. L. M. Doubova, S. Trasatti and S. Valcher, *J. Electroanal. Chem.*, 1993, **349**, 187-195.
92. S. Trasatti and E. Lust, in *Modern aspects of electrochemistry*, Springer, 2002, pp. 1-215.
93. J. Chen, L. Nie and S. Yao, *J. Electroanal. Chem.*, 1996, **414**, 53-59.
94. J.-H. Chen, S.-H. Si, L.-H. Nie and S.-Z. Yao, *Electrochim. Acta*, 1997, **42**, 689-695.
95. Q. Zha, *Science, Beijing*, 2002, 339.
96. D. D. Bode, T. N. Andersen and H. Eyring, *J. Phys. Chem.*, 1967, **71**, 792-797.
97. G. Valette, *J. Electroanal. Chem. Interfacial Electrochem.*, 1989, **269**, 191-203.
98. T. Vitanov, A. Popov and E. S. Sevastyanov, *J. Electroanal. Chem. Interfacial Electrochem.*, 1982, **142**, 289-297.
99. A. Hamelin and G. Valette, *COMPTES RENDUS HEBDOMADAIRES DES SEANCES DE L ACADEMIE DES SCIENCES SERIE C*, 1969, **269**, 1020-&.
100. G. Valette and A. Hamelin, *COMPTES RENDUS HEBDOMADAIRES DES SEANCES DE L ACADEMIE DES SCIENCES SERIE C*, 1971, **272**, 602-&.
101. G. Valette, *J. Electroanal. Chem. Interfacial Electrochem.*, 1982, **138**, 37-54.
102. A. Hamelin, T. Vitanov, E. Sevastyanov and A. Popov, *J. Electroanal. Chem. Interfacial Electrochem.*, 1983, **145**, 225-264.
103. S. Trasatti and L. M. Doubova, *J. Chem. Soc., Faraday Trans.*, 1995, **91**, 3311-3325.
104. G. Valette, 1982.
105. M. Bacchetta, A. Francesconi, S. Trasatti, L. Doubova and A. Hamelin, *J. Electroanal. Chem. Interfacial Electrochem.*, 1987, **218**, 355-360.

106. D. Kolb, A. Dakkouri and N. Batina, in *Nanoscale Probes of the Solid/Liquid Interface*, Springer, 1995, pp. 263-284.
107. D. M. Kolb and J. Schneider, *Electrochim. Acta*, 1986, **31**, 929-936.
108. P. Carles, A. Cazabat and E. Kolb, *Colloids Surf., A*, 1993, **79**, 65-70.
109. U. W. Hamm, D. Kramer, R. S. Zhai and D. M. Kolb, *J. Electroanal. Chem.*, 1996, **414**, 85-89.
110. J. J. Calvente, Z. Kováčová, R. Andreu and W. R. Fawcett, *J. Electroanal. Chem.*, 1996, **401**, 231-235.
111. A. Hamelin, *J. Electroanal. Chem.*, 1995, **386**, 1-10.
112. T. N. Anderson, J. L. Anderson and H. Eyring, *J. Phys. Chem.*, 1969, **73**, 3562-3570.
113. P. Caswell, N. A. Hampson and D. Larkin, *J. Electroanal. Chem.*, 1969, **20**, 335-338.
114. Y. Ipatov, V. Batrakov and V. Shalaginov, *Elektrokhimiya*, 1976, **12**, 286-290.
115. V. V. Batrakov and B. B. Damaskin, *J. Electroanal. Chem. Interfacial Electrochem.*, 1975, **65**, 361-372.
116. T. Lezhava, B. Tsanava and M. Kikabidze, 1975.
117. T. Andersen, R. Perkins and H. Eyring, *J. Am. Chem. Soc.*, 1964, **86**, 4496-4496.
118. I. Novoselsky, N. Maksimyuk and L. Egorov, *Elektrokhimiya*, 1973, **9**, 1518-1523.
119. J. Lecoeur and J. P. Bellier, *Electrochim. Acta*, 1985, **30**, 1027-1033.
120. D. Golub, A. Soffer and Y. Oren, *J. Electroanal. Chem. Interfacial Electrochem.*, 1989, **260**, 383-392.
121. J. Poon, C. Batchelor-McAuley, K. Tschulik and R. G. Compton, *Chem. Sci.*, 2015, **6**, 2869-2876.
122. M. W. J. Prins, W. J. J. Welters and J. W. Weekamp, *Science*, 2001, **291**, 277-280.
123. T. B. Jones, *Langmuir*, 2002, **18**, 4437-4443.
124. R. Digilov, *Langmuir*, 2000, **16**, 6719-6723.
125. M. Li, X. Tian, S. Garg, T. E. Rufford, P. Zhao, Y. Wu, A. J. Yago, L. Ge, V. Rudolph and G. Wang, *ACS Appl. Mater. Interfaces*, 2020, **12**, 22760-22770.
126. M. Li, M. N. Idros, Y. Wu, S. Garg, S. Gao, R. Lin, H. Rabiee, Z. Li, L. Ge, T. E. Rufford, Z. Zhu, L. Li and G. Wang, *React. Chem. Eng.*, 2021, **6**, 345-352.
127. S. Garg, M. Li, Y. Wu, M. Nazmi Idros, H. Wang, A. J. Yago, L. Ge, G. G. X. Wang and T. E. Rufford, *ChemSusChem*, 2021, **14**, 2601-2611.
128. S. Garg, M. Li, T. E. Rufford, L. Ge, V. Rudolph, R. Knibbe, M. Konarova and G. G. X. Wang, *ChemSusChem*, 2020, **13**, 304-311.
129. S. H. Lee, J. C. Lin, M. Farmand, A. T. Landers, J. T. Feaster, J. E. Avilés Acosta, J. W. Beeman, Y. Ye, J. Yano, A. Mehta, R. C. Davis, T. F. Jaramillo, C. Hahn and W. S. Drisdell, *J. Am. Chem. Soc.*, 2021, **143**, 588-592.
130. J. Huang, N. Hörmann, E. Oveisi, A. Loiudice, G. L. De Gregorio, O. Andreussi, N. Marzari and R. Buonsanti, *Nat. Commun.*, 2018, **9**, 3117.
131. R. M. Arán-Ais, R. Rizo, P. Grosse, G. Algara-Siller, K. Dembélé, M. Plodinec, T. Lunkenbein, S. W. Chee and B. R. Cuenya, *Nat. Commun.*, 2020, **11**, 3489.
132. J.-J. Velasco-Velez, R. V. Mom, L.-E. Sandoval-Diaz, L. J. Falling, C.-H. Chuang, D. Gao, T. E. Jones, Q. Zhu, R. Arrigo, B. Roldan Cuenya, A. Knop-Gericke, T. Lunkenbein and R. Schlögl, *ACS Energy Lett.*, 2020, **5**, 2106-2111.
133. G. S. Shapoval, A. A. Pud, P. V. Zamotayev and A. A. Kachan, *Polymer Science U.S.S.R.*, 1985, **27**, 2427-2431.
134. J. T. Gostick, M. W. Fowler, M. A. Ioannidis, M. D. Pritzker, Y. M. Volfkovich and A. Sakars, *J. Power Sources*, 2006, **156**, 375-387.
135. D. Wakerley, S. Lamaison, F. Ozanam, N. Menguy, D. Mercier, P. Marcus, M. Fontecave and V. Mougel, *Nat. Mater.*, 2019, **18**, 1222-1227.
136. J. Li, G. Chen, Y. Zhu, Z. Liang, A. Pei, C.-L. Wu, H. Wang, H. R. Lee, K. Liu, S. Chu and Y. Cui, *Nat. Catal.*, 2018, **1**, 592-600.
137. R. Shi, J. Guo, X. Zhang, G. I. N. Waterhouse, Z. Han, Y. Zhao, L. Shang, C. Zhou, L. Jiang and T. Zhang, *Nat. Commun.*, 2020, **11**, 3028.

138. G. Park, S. Hong, M. Choi, S. Lee and J. Lee, *Catal. Today*, 2020, **355**, 340-346.
139. M. Jouny, W. Luc and F. Jiao, *Nat. Catal.*, 2018, **1**, 748-755.
140. M. Favaro, H. Xiao, T. Cheng, W. A. Goddard, J. Yano and E. J. Crumlin, *Proc. Natl. Acad. Sci.*, 2017, DOI: 10.1073/pnas.1701405114, 201701405.
141. O. A. Moultos, I. N. Tsimpanogiannis, A. Z. Panagiotopoulos and I. G. Economou, *J. Phys. Chem. B*, 2014, **118**, 5532-5541.
142. F. P. García de Arquer, C.-T. Dinh, A. Ozden, J. Wicks, C. McCallum, A. R. Kirmani, D.-H. Nam, C. Gabardo, A. Seifitokaldani, X. Wang, Y. C. Li, F. Li, J. Edwards, L. J. Richter, S. J. Thorpe, D. Sinton and E. H. Sargent, *Science*, 2020, **367**, 661-666.
143. M. R. Singh, E. L. Clark and A. T. Bell, *Phys. Chem. Chem. Phys.*, 2015, **17**, 18924-18936.
144. E. L. Clark, J. Resasco, A. Landers, J. Lin, L.-T. Chung, A. Walton, C. Hahn, T. F. Jaramillo and A. T. Bell, *ACS Catal.*, 2018, **8**, 6560-6570.
145. Z. Xing, L. Hu, D. S. Ripatti, X. Hu and X. Feng, *Nat. Commun.*, 2021, **12**, 136.
146. K. Junge Puring, D. Siegmund, J. Timm, F. Möllenbruck, S. Schemme, R. Marschall and U.-P. Apfel, *Adv. Sustainable Syst.*, 2021, **5**, 2000088.
147. J. Wu, P. P. Sharma, B. H. Harris and X.-D. Zhou, *J. Power Sources*, 2014, **258**, 189-194.
148. D. McLaughlin, M. Bierling, R. Moroni, C. Vogl, G. Schmid and S. Thiele, *Adv. Energy Mater.*, 2020, **10**, 2000488.
149. Z. Qi, M. M. Biener, A. R. Kashi, S. Hunegnaw, A. Leung, S. Ma, Z. Huo, K. P. Kuhl and J. Biener, *Mater. Res. Lett.*, 2021, **9**, 99-104.
150. Z. Xing, X. Hu and X. Feng, *ACS Energy Lett.*, 2021, **Advance Article**, 1694-1702.
151. A. Löwe, M. Schmidt, F. Bienen, D. Kopljar, N. Wagner and E. Klemm, *ACS Sustainable Chem. Eng.*, 2021, **9**, 4213-4223.
152. X. Li, F. Feng, K. Zhang, S. Ye, D. Y. Kwok and V. Birss, *Langmuir*, 2012, **28**, 6698-6705.
153. Q. Wang, H. Dong, H. Yu and H. Yu, *J. Power Sources*, 2015, **279**, 1-5.
154. H.-Q. Liang, S. Zhao, X.-M. Hu, M. Ceccato, T. Skrydstrup and K. Daasbjerg, *ACS Catal.*, 2021, **11**, 958-966.
155. M. E. Leonard, M. J. Orella, N. Aiello, Y. Román-Leshkov, A. Forner-Cuenca and F. R. Brushett, *J. Electrochem. Soc.*, 2020, **167**, 124521.
156. P. K. Weissenborn and R. J. Pugh, *Langmuir*, 1995, **11**, 1422-1426.
157. L. M. Pegram and M. T. Record, *J. Phys. Chem. B*, 2007, **111**, 5411-5417.
158. K. Ali, A.-u.-H. A. Shah, S. Bilal and A.-u.-H. A. Shah, *Colloids Surf., A*, 2009, **337**, 194-199.
159. D. Gao, F. Scholten and B. Roldan Cuenya, *ACS Catal.*, 2017, **7**, 5112-5120.
160. S. Garg, M. Li, Y. Wu, M. N. Idros, H. Wang, Y. Anya Josefa, L. Ge, G. G. X. Wang and T. E. Rufford, *ChemSusChem*, **Advance Article**
161. A. S. Varela, W. Ju, T. Reier and P. Strasser, *ACS Catal.*, 2016, **6**, 2136-2144.
162. S. Lee, D. Kim and J. Lee, *Angew. Chem., Int. Ed. Engl.*, 2015, **54**, 14701-14705.
163. V. J. Ovalle and M. M. Waegele, *J. Phys. Chem. C*, 2020, **124**, 14713-14721.
164. R. Zangi and J. B. F. N. Engberts, *J. Am. Chem. Soc.*, 2005, **127**, 2272-2276.
165. R. Zimmermann, S. Dukhin and C. Werner, *J. Phys. Chem. B*, 2001, **105**, 8544-8549.
166. A. Quinn, R. Sedev and J. Ralston, *J. Phys. Chem. B*, 2003, **107**, 1163-1169.
167. M. E. Schrader, *J. Colloid Interface Sci.*, 1984, **100**, 372-380.
168. S. Gim, K. J. Cho, H.-K. Lim and H. Kim, *Sci. Rep.*, 2019, **9**, 14805.
169. T. Sarkar, S. Ghosh, M. Annamalai, A. Patra, K. Stoerzinger, Y.-L. Lee, S. Prakash, M. R. Motapothula, Y. Shao-Horn, L. Giordano and T. Venkatesan, *RSC Advances*, 2016, **6**, 109234-109240.
170. Y. Kuang, G. Feng, P. Li, Y. Bi, Y. Li and X. Sun, *Angew. Chem., Int. Ed. Engl.*, 2016, **55**, 693-697.
171. Z. Lu, W. Zhu, X. Yu, H. Zhang, Y. Li, X. Sun, X. Wang, H. Wang, J. Wang, J. Luo, X. Lei and L. Jiang, *Adv. Mater. (Weinheim, Ger.)*, 2014, **26**, 2683-2687.
172. G. B. Darband, M. Aliofkhazraei and S. Shanmugam, *Renewable and Sustainable Energy Reviews*, 2019, **114**, 109300.

173. Y. Wang, H. Su, Y. He, L. Li, S. Zhu, H. Shen, P. Xie, X. Fu, G. Zhou, C. Feng, D. Zhao, F. Xiao, X. Zhu, Y. Zeng, M. Shao, S. Chen, G. Wu, J. Zeng and C. Wang, *Chem. Rev.*, 2020, **120**, 12217-12314.
174. X.-L. Lu, X. Rong, C. Zhang and T.-B. Lu, *J. Mater. Chem. A*, 2020, **8**, 10695-10708.
175. Y. Huang, Y. Jiao, T. Chen, Y. Gong, S. Wang, Y. Liu, D. S. Sholl and K. S. Walton, *ACS Appl. Mater. Interfaces*, 2020, **12**, 34413-34422.
176. L. Jiao, Y. Wang, H.-L. Jiang and Q. Xu, *Adv. Mater. (Weinheim, Ger.)*, 2018, **30**, 1703663.
177. D.-H. Nam, O. S. Bushuyev, J. Li, P. De Luna, A. Seifitokaldani, C.-T. Dinh, F. P. García de Arquer, Y. Wang, Z. Liang, A. H. Proppe, C. S. Tan, P. Todorović, O. Shekhah, C. M. Gabardo, J. W. Jo, J. Choi, M.-J. Choi, S.-W. Baek, J. Kim, D. Sinton, S. O. Kelley, M. Eddaoudi and E. H. Sargent, *J. Am. Chem. Soc.*, 2018, **140**, 11378-11386.
178. C. Yan, H. Li, Y. Ye, H. Wu, F. Cai, R. Si, J. Xiao, S. Miao, S. Xie, F. Yang, Y. Li, G. Wang and X. Bao, *Energy Environ. Sci.*, 2018, **11**, 1204-1210.
179. Y. Cheng, S. Zhao, H. Li, S. He, J.-P. Veder, B. Johannessen, J. Xiao, S. Lu, J. Pan, M. F. Chisholm, S.-Z. Yang, C. Liu, J. G. Chen and S. P. Jiang, *Appl. Catal., B*, 2019, **243**, 294-303.
180. S. Qiu, C. A. Fuentes, D. Zhang, A. W. Van Vuure and D. Seveno, *Langmuir*, 2016, **32**, 9697-9705.
181. R. H. Bradley and P. Pendleton, *Adsorpt. Sci. Technol.*, 2013, **31**, 113-133.
182. X. Wang, A. Xu, F. Li, S.-F. Hung, D.-H. Nam, C. M. Gabardo, Z. Wang, Y. Xu, A. Ozden, A. S. Rasouli, A. H. Ip, D. Sinton and E. H. Sargent, *J. Am. Chem. Soc.*, 2020, **142**, 3525-3531.
183. H. Pan and C. J. Barile, *Energy Environ. Sci.*, 2020, **13**, 3567-3578.
184. S. Perry, S. Mavrikis, M. Wegener, P. Nazarovs, L. Wang and C. Ponce de Leon, *Faraday Discuss.*, 2021, **Advance Article**.
185. S. Goswami, S. Klaus and J. Benziger, *Langmuir*, 2008, **24**, 8627-8633.
186. T. Mabuchi, S.-F. Huang and T. Tokumasu, *Macromolecules*, 2021, **54**, 115-125.
187. D. Hursán, A. A. Samu, L. Janovák, K. Artyushkova, T. Asset, P. Atanassov and C. Janáky, *Joule*, 2019, **3**, 1719-1733.
188. T. Burdyny, P. J. Graham, Y. Pang, C.-T. Dinh, M. Liu, E. H. Sargent and D. Sinton, *ACS Sustainable Chem. Eng.*, 2017, **5**, 4031-4040.
189. Y.-G. Kim, A. Javier, J. H. Baricuatro, D. Torelli, K. D. Cummins, C. F. Tsang, J. C. Hemminger and M. P. Soriaga, *J. Electroanal. Chem.*, 2016, **780**, 290-295.
190. G. H. Simon, C. S. Kley and B. Roldan Cuenya, *Angew. Chem., Int. Ed. Engl.*, 2021, **60**, 2561-2568.
191. R. M. Arán-Ais, F. Scholten, S. Kunze, R. Rizo and B. Roldan Cuenya, *Nat. Energy*, 2020, **5**, 317-325.
192. W. Ma, S. Xie, T. Liu, Q. Fan, J. Ye, F. Sun, Z. Jiang, Q. Zhang, J. Cheng and Y. Wang, *Nat. Catal.*, 2020, **3**, 478-487.
193. S. Sen, S. M. Brown, M. Leonard and F. R. Brushett, *J. Appl. Electrochem.*, 2019, **49**, 917-928.
194. H. Yang, Q. Lin, C. Zhang, X. Yu, Z. Cheng, G. Li, Q. Hu, X. Ren, Q. Zhang, J. Liu and C. He, *Nat. Commun.*, 2020, **11**, 593.
195. W.-H. Cheng, M. H. Richter, I. Sullivan, D. M. Larson, C. Xiang, B. S. Brunschwig and H. A. Atwater, *ACS Energy Lett.*, 2020, **5**, 470-476.
196. Y.-L. Qiu, H.-X. Zhong, T.-T. Zhang, W.-B. Xu, P.-P. Su, X.-F. Li and H.-M. Zhang, *ACS Appl. Mater. Interfaces*, 2018, **10**, 2480-2489.
197. J. Zhang, W. Luo and A. Züttel, *J. Mater. Chem. A*, 2019, **7**, 26285-26292.
198. C.-T. Dinh, F. P. García de Arquer, D. Sinton and E. H. Sargent, *ACS Energy Lett.*, 2018, **3**, 2835-2840.
199. Y. Wang, Z. Wang, C.-T. Dinh, J. Li, A. Ozden, M. Golam Kibria, A. Seifitokaldani, C.-S. Tan, C. M. Gabardo, M. Luo, H. Zhou, F. Li, Y. Lum, C. McCallum, Y. Xu, M. Liu, A. Proppe, A. Johnston, P. Todorovic, T.-T. Zhuang, D. Sinton, S. O. Kelley and E. H. Sargent, *Nat. Catal.*, 2020, **3**, 98-106.

200. F. Li, A. Thevenon, A. Rosas-Hernández, Z. Wang, Y. Li, C. M. Gabardo, A. Ozden, C. T. Dinh, J. Li, Y. Wang, J. P. Edwards, Y. Xu, C. McCallum, L. Tao, Z.-Q. Liang, M. Luo, X. Wang, H. Li, C. P. O'Brien, C.-S. Tan, D.-H. Nam, R. Quintero-Bermudez, T.-T. Zhuang, Y. C. Li, Z. Han, R. D. Britt, D. Sinton, T. Agapie, J. C. Peters and E. H. Sargent, *Nature*, 2020, **577**, 509-513.
201. A. Ozden, F. Li, F. P. García de Arquer, A. Rosas-Hernández, A. Thevenon, Y. Wang, S.-F. Hung, X. Wang, B. Chen, J. Li, J. Wicks, M. Luo, Z. Wang, T. Agapie, J. C. Peters, E. H. Sargent and D. Sinton, *ACS Energy Lett.*, 2020, **5**, 2811-2818.
202. Y. Xu, J. P. Edwards, J. Zhong, C. P. O'Brien, C. M. Gabardo, C. McCallum, J. Li, C.-T. Dinh, E. H. Sargent and D. Sinton, *Energy Environ. Sci.*, 2020, **13**, 554-561.
203. J. Wicks, M. L. Jue, V. A. Beck, J. S. Oakdale, N. A. Dudukovic, A. L. Clemens, S. Liang, M. E. Ellis, G. Lee, S. E. Baker, E. B. Duoss and E. H. Sargent, *Adv. Mater. (Weinheim, Ger.)*, 2021, **33**, 2003855.
204. X. Yan, C. Chen, Y. Wu, S. Liu, Y.-Z. Chen, R. Feng, J. Zhang and B. Han, *Chem. Sci.*, 2021, **Advance Article**.
205. Y. C. Tan, K. B. Lee, H. Song and J. Oh, *Joule*, 2020, **4**, 1104-1120.
206. X. Xuan, S. Chen, S. Zhao, J. Y. Yoon, G. Boczkaj and X. Sun, *Front. chem.*, 2020, **8**.
207. W. Choi, D. H. Won and Y. J. Hwang, *J. Mater. Chem. A*, 2020, **8**, 15341-15357.
208. Y. Zhu, X. Yang, C. Peng, C. Priest, Y. Mei and G. Wu, *Small*, **17**, 2005148.
209. F. Pan and Y. Yang, *Energy Environ. Sci.*, 2020, **13**, 2275-2309.
210. D. Voiry, H. S. Shin, K. P. Loh and M. Chhowalla, *Nat. Rev. Chem.*, 2018, **2**, 0105.
211. C. Zhao, Y. Wang, Z. Li, W. Chen, Q. Xu, D. He, D. Xi, Q. Zhang, T. Yuan, Y. Qu, J. Yang, F. Zhou, Z. Yang, X. Wang, J. Wang, J. Luo, Y. Li, H. Duan, Y. Wu and Y. Li, *Joule*, 2019, **3**, 584-594.
212. R. Chen, W. Tian, Y. Jia, W. Xu, F. Chen, X. Duan, Q. Xie, C. Hu, W. Liu, Y. Zhao, Y. Kuang, Y. Zhang and X. Sun, *ACS Appl. Energy Mater.*, 2019, **2**, 3991-3998.
213. Y. Song, J. R. C. Junqueira, N. Sikdar, D. Öhl, S. Dieckhöfer, T. Quast, S. Seisel, J. Masa, C. Andronescu and W. Schuhmann, *Angew. Chem., Int. Ed. Engl.*, **n/a**.
214. A. Reyes, R. P. Jansonius, B. A. W. Mowbray, Y. Cao, D. G. Wheeler, J. Chau, D. J. Dvorak and C. P. Berlinguette, *ACS Energy Lett.*, 2020, **5**, 1612-1618.
215. W. Zhang, J. Ma, P. Wang, Z. Wang, F. Shi and H. Liu, *J. Membr. Sci.*, 2016, **502**, 37-47.
216. E. W. Lees, B. A. W. Mowbray, D. A. Salvatore, G. L. Simpson, D. J. Dvorak, S. Ren, J. Chau, K. L. Milton and C. P. Berlinguette, *J. Mater. Chem. A*, 2020, **8**, 19493-19501.
217. A. Kusoglu and A. Z. Weber, *Chem. Rev.*, 2017, **117**, 987-1104.
218. C.-H. Ma, T. L. Yu, H.-L. Lin, Y.-T. Huang, Y.-L. Chen, U. S. Jeng, Y.-H. Lai and Y.-S. Sun, *Polymer*, 2009, **50**, 1764-1777.
219. J. H. Lee, G. Doo, S. H. Kwon, S. Choi, H.-T. Kim and S. G. Lee, *Sci. Rep.*, 2018, **8**, 10739.
220. Y. Guo, F. Pan, W. Chen, Z. Ding, D. Yang, B. Li, P. Ming and C. Zhang, *Electrochem. Energy Rev.*, 2021, **4**, 67-100.
221. C.-Y. Ahn, J. Ahn, S. Y. Kang, O.-H. Kim, D. W. Lee, J. H. Lee, J. G. Shim, C. H. Lee, Y.-H. Cho and Y.-E. Sung, *Science Advances*, 2020, **6**, eaaw0870.
222. D. Yang, H. Yu, G. Li, Y. Zhao, Y. Liu, C. Zhang, W. Song and Z. Shao, *J. Power Sources*, 2014, **267**, 39-47.
223. J. Zhang, Y. Pei, W. Zhu, Y. Liu, Y. Yin, Y. Qin and M. D. Guiver, *J. Power Sources*, 2021, **484**, 229259.
224. T.-H. Kim, J.-Y. Yi, C.-Y. Jung, E. Jeong and S.-C. Yi, *Int. J. Hydrogen Energy*, 2017, **42**, 478-485.
225. R. S. Yeo, *Polymer*, 1980, **21**, 432-435.
226. M. Chisaka, E. Matsuoka and H. Daiguji, *J. Electrochem. Soc.*, 2010, **157**, B1218.
227. H.-R. M. Jhong, F. R. Brushett and P. J. A. Kenis, *Adv. Energy Mater.*, 2013, **3**, 589-599.
228. A. K. Buckley, M. Lee, T. Cheng, R. V. Kazantsev, D. M. Larson, W. A. Goddard Iii, F. D. Toste and F. M. Toma, *J. Am. Chem. Soc.*, 2019, **141**, 7355-7364.
229. Z. Cai, Y. Zhang, Y. Zhao, Y. Wu, W. Xu, X. Wen, Y. Zhong, Y. Zhang, W. Liu, H. Wang, Y. Kuang and X. Sun, *Nano Research*, 2019, **12**, 345-349.

230. P. An, L. Wei, H. Li, B. Yang, K. Liu, J. Fu, H. Li, H. Liu, J. Hu, Y.-R. Lu, H. Pan, T.-S. Chan, N. Zhang and M. Liu, *J. Mater. Chem. A*, 2020, **8**, 15936-15941.
231. Z. Han, R. Kortlever, H.-Y. Chen, J. C. Peters and T. Agapie, *ACS Central Science*, 2017, **3**, 853-859.
232. C. Kim, H. S. Jeon, T. Eom, M. S. Jee, H. Kim, C. M. Friend, B. K. Min and Y. J. Hwang, *J. Am. Chem. Soc.*, 2015, **137**, 13844-13850.
233. Y. Zhao, C. Wang, Y. Liu, D. R. MacFarlane and G. G. Wallace, *Adv. Energy Mater.*, 2018, **8**, 1801400.
234. Z. Cao, J. S. Derrick, J. Xu, R. Gao, M. Gong, E. M. Nichols, P. T. Smith, X. Liu, X. Wen, C. Copéret and C. J. Chang, *Angew. Chem., Int. Ed. Engl.*, 2018, **57**, 4981-4985.
235. Y. Fang and J. C. Flake, *J. Am. Chem. Soc.*, 2017, **139**, 3399-3405.
236. M. S. Xie, B. Y. Xia, Y. Li, Y. Yan, Y. Yang, Q. Sun, S. H. Chan, A. Fisher and X. Wang, *Energy Environ. Sci.*, 2016, **9**, 1687-1695.
237. S. Ahn, K. Klyukin, R. J. Wakeham, J. A. Rudd, A. R. Lewis, S. Alexander, F. Carla, V. Alexandrov and E. Andreoli, *ACS Catal.*, 2018, **8**, 4132-4142.
238. X. Wei, Z. Yin, K. Lyu, Z. Li, J. Gong, G. Wang, L. Xiao, J. Lu and L. Zhuang, *ACS Catal.*, 2020, **10**, 4103-4111.
239. Y. Zhong, Y. Xu, J. Ma, C. Wang, S. Sheng, C. Cheng, M. Li, L. Han, L. Zhou, Z. Cai, Y. Kuang, Z. Liang and X. Sun, *Angew. Chem., Int. Ed. Engl.*, 2020, **59**, 19095-19101.
240. S. Banerjee, X. Han and V. S. Thoi, *ACS Catal.*, 2019, **9**, 5631-5637.
241. X. Chen, J. Chen, N. M. Alghoraibi, D. A. Henckel, R. Zhang, U. O. Nwabara, K. E. Madsen, P. J. A. Kenis, S. C. Zimmerman and A. A. Gewirth, *Nat. Catal.*, 2021, **4**, 20-27.
242. A. Thevenon, A. Rosas-Hernández, J. C. Peters and T. Agapie, *Angew. Chem., Int. Ed. Engl.*, 2019, **58**, 16952-16958.
243. T. Cheng, L. Wang, B. V. Merinov and W. A. Goddard, *J. Am. Chem. Soc.*, 2018, **140**, 7787-7790.
244. T. Cheng, H. Xiao and W. A. Goddard, *J. Am. Chem. Soc.*, 2016, **138**, 13802-13805.
245. Z.-Q. Zhang, S. Banerjee, V. S. Thoi and A. Shoji Hall, *J. Phys. Chem. Lett.*, 2020, **11**, 5457-5463.
246. J. Wang, T. Cheng, A. Q. Fenwick, T. N. Baroud, A. Rosas-Hernández, J. H. Ko, Q. Gan, W. A. Goddard Iii and R. H. Grubbs, *J. Am. Chem. Soc.*, 2021, **143**, 2857-2865.
247. A. Z. Weber, *J. Power Sources*, 2010, **195**, 5292-5304.
248. J. Yin, W. Zhang, N. A. Alhebshi, N. Salah and H. N. Alshareef, *Small Methods*, 2020, **4**, 1900853.
249. H. Wang, Y. Shao, S. Mei, Y. Lu, M. Zhang, J.-k. Sun, K. Matyjaszewski, M. Antonietti and J. Yuan, *Chem. Rev.*, 2020, **120**, 9363-9419.
250. H. Liu, S. Wu, N. Tian, F. Yan, C. You and Y. Yang, *J. Mater. Chem. A*, 2020, **8**, 23699-23723.
251. M. Breitwieser, M. Klingele, S. Vierrath, R. Zengerle and S. Thiele, *Adv. Energy Mater.*, 2018, **8**, 1701257.
252. S. Du, *Engineering*, 2021, **7**, 33-49.
253. B. Endrődi, E. Kecsenovity, A. Samu, F. Darvas, R. V. Jones, V. Török, A. Danyi and C. Janáky, *ACS Energy Lett.*, 2019, **4**, 1770-1777.
254. W. H. Lee, C. Lim, S. Y. Lee, K. H. Chae, C. H. Choi, U. Lee, B. K. Min, Y. J. Hwang and H.-S. Oh, *Nano Energy*, 2021, **84**, 105859.
255. A. Ozden, Y. Wang, F. Li, M. Luo, J. Sisler, A. Thevenon, A. Rosas-Hernández, T. Burdyny, Y. Lum, H. Yadegari, T. Agapie, J. C. Peters, E. H. Sargent and D. Sinton, *Joule*, 2021, **5**, 706-719.
256. Z. Gu, H. Shen, Z. Chen, Y. Yang, C. Yang, Y. Ji, Y. Wang, C. Zhu, J. Liu, J. Li, T.-K. Sham, X. Xu and G. Zheng, *Joule*, 2021, **5**, 429-440.
257. L.-C. Weng, A. T. Bell and A. Z. Weber, *Energy Environ. Sci.*, 2020, **13**, 3592-3606.
258. J. C. Fornaciari, M. R. Gerhardt, J. Zhou, Y. N. Regmi, N. Danilovic, A. T. Bell and A. Z. Weber, *J. Electrochem. Soc.*, 2020, **167**, 104508.